INTERNATIONAL JOURNAL FOR NUMERICAL METHODS IN ENGINEERING
Int. J. Numer. Meth. Engng 2011; **87**:566–592
Published online 23 January 2011 in Wiley Online Library (wileyonlinelibrary.com). DOI: 10.1002/nme.3122

A spectral element approach for the stability of delay systems

Firas A. Khasawneh*, † and Brian P. Mann

Mechanical Engineering and Materials Science Department, Duke University, Durham, NC 27705, U.S.A.

SUMMARY

We describe a spectral element approach to study the stability and equilibria solutions of Delay differential equations (DDEs). In contrast to the prototypical temporal finite element analysis (TFEA), the described spectral element approach admits spectral rates of convergence and allows exploiting *hp*-convergence schemes. The described approach also avoids the limitations of analytical integrations in TFEA by using highly accurate numerical quadratures—enabling the study of more complicated DDEs. The effectiveness of this new approach is compared with well-established methods in the literature using various case studies. Specifically, the stability results are compared with the conventional TFEA and Legendre collocation methods whereas the equilibria solutions are compared with the numerical simulations and the homotopy perturbation method (HPM) solutions. Our results reveal that the presented approach can have higher rates of convergence than both collocation methods and the HPM. Copyright © 2011 John Wiley & Sons, Ltd.

Received 29 December 2009; Revised 26 October 2010; Accepted 6 November 2010

KEY WORDS: delay equations; high-order trial functions; homotopy perturbation method; Legendre points; spectral element; temporal finite element analysis

1. INTRODUCTION

Delay differential equations (DDEs) have been used widely to model physical and biological phenomena [1]. Some examples include machining dynamics [2, 3], laser systems [4, 5], coupled delay-line oscillators [6], traffic models [7, 8], and human balance [9, 10]. However, although the inclusion of delays often leads to more realistic models, the resulting infinite-dimensional state–space significantly complicates the analysis [11, 12]. The interest in studying DDEs often lies in calculating the equilibria solutions and determining their stability. However, since delays result in an infinite-dimensional state–space, it is often necessary to use approximate procedures to calculate the solutions and ascertain their stability.

Many analysis methods have appeared in the literature for studying delay equations. For example, the stability of DDEs has been studied using D-subdivision [11], continuous time approximation (CTA) [13–15], and the cluster treatment of characteristic roots methods (CTCR) [16, 17]. The focus in D-subdivision and the CTCR methods is on charting the stability boundaries by investigating the DDE's characteristic polynomial. Whereas CTCR can find the stability of a wide class of autonomous delay equations, the D-subdivision method is confined to a much smaller class of DDEs, namely systems with no or very small damping [11].

On the other hand, the CTA method converts the DDE into an equivalent high and finite-dimensional state–space. Therefore, it can yield both the stability and equilibria of the underlying DDE. Nevertheless, for some DDEs the CTA method can produce very large matrices leading

*Correspondence to: Firas A. Khasawneh, Mechanical Engineering and Materials Science Department, Duke University, Durham, NC 27708, U.S.A.
†E-mail: firas.khasawneh@duke.edu

to significant computational difficulties. In addition, many issues regarding the convergence and numerical stability of CTA have not yet been addressed. A common limitation of all the above methods is that they have only been applicable to autonomous delay equations and alternative methods need to be used for non-autonomous DDEs.

Recently, the homotopy perturbation method (HPM) [18–21] and the variational iteration method (VIM) [21–24] were developed to find approximate analytical solutions for differential equations. These two methods have also been successfully applied to non-autonomous delay equations in References [25–28]. In many cases, the solutions obtained using VIM [29] or HPM [19, 30] converge after only a few iterations for a suitable choice of the initial solution [31]. However, although these methods are powerful tools for obtaining solutions of functional differential equations, they do not provide any information on the stability of equilibria and additional steps are needed to determine stability. Nevertheless, in this study, the solutions obtained using HPM and spectral element approach will be compared with numerical simulations.

Examples of other methods that can be used for autonomous as well as non-autonomous DDEs include the semi-discretization method [32, 33], collocation-based methods [34–38], and temporal finite element analysis (TFEA) [39].

The semi-discretization method divides the time-line into short intervals on which an approximate analytical solution can be obtained. The collection of these expressions can then be used to create a finite-dimensional transition matrix, which approximates the infinite-dimensional monodromy operator of the DDE. However, the semi-discretization method, similar to the closely related CTA method, can result in large matrices to produce a convergent solution. Further, a large number of matrix operations might be necessary—especially for time-periodic systems with incommensurate period and delays [33].

Collocation methods are a type of weighted residual approach with Dirac delta trial functions [40]. These methods typically use a discretization based on Chebyshev or Legendre points to construct a dynamic map that approximates the DDE. The characteristic multipliers, i.e. eigenvalues, of the map are then analyzed to ascertain stability. In addition, the dynamic map—along with a specified initial function—can be used to propagate the solution at the discretization points one period at a time. Collocation methods have been successful in studying a wide class of delay equations and a proof of their convergence can be found in Reference [36]. However, a recent study concluded that better convergence rates can be achieved if the weighted residual approach is instead combined with high-order trial functions (i.e. a high-order Galerkin-type approach) [41].

One Galerkin-type approach is the TFEA which has been used to study the stability of equilibria in linear DDEs [42–44]. In comparison with many other discretization methods, TFEA could easily handle DDEs with piecewise continuous coefficients. In TFEA, the time interval of interest is discretized into a finite number of temporal elements. The original DDE is then transformed into the form of a discrete map whose characteristic multipliers determine stability. The initial formulation of TFEA restricted the approach to at most second-order DDEs [42, 45]. However, in Reference [39] the technique was generalized to linear DDEs with a single discrete delay and the improved approach was called state–space TFEA.

Although the state–space TFEA was successful in extending the usefulness of TFEA to a broader class of DDEs, it still suffered from several key limitations. Specifically, state–space TFEA relied mostly on increasing the number of elements to achieve convergence, i.e. h-convergence. This limited the approach to the slower linear rates of convergence as opposed to the fast exponential rates observed in some collocation methods. The inability to achieve spectral convergence, or p-convergence, was due to the inefficient choice of the trial functions. For historic reasons, these functions were obtained through Hermite interpolation on equidistant nodes, as will be shown in Section 3. Owing to this choice, increasing the order of the trial functions was impractical and further lead to an ill-conditioned system. In addition, the state–space TFEA approach applied analytical integration to generate the weighted residual equations. The integration was performed using a software with symbolic manipulation capabilities; however, this was often computationally expensive especially for systems with complicated time-dependent coefficients, where closed-form

DOI: 10.1002/nme

integrals could not be obtained. Relying on analytical integration and h-convergence alone prevented the conventional TFEA approach from handling more general delay equations.

In this paper we describe a spectral element approach to study the stability and equilibria solutions of DDEs. In contrast to the conventional state–space TFEA, the developed spectral element approach can have exponential rates of convergence and it admits hp-convergence schemes. The described spectral element approach also avoids the limitations of analytical integrations in state–space TFEA by applying highly accurate numerical quadratures—enabling the study of more complicated DDEs. The efficiency of this new approach is compared with well-established methods in the literature using various case studies. Specifically, stability results are compared with the conventional state–space TFEA and Legendre collocation methods whereas the equilibria solutions are compared with the numerical simulations and HPM. Our results reveal that the presented approach can have higher rates of convergence than both collocation methods and the HPM.

This paper is organized as follows: Section 2 describes the general procedure in the TFEA approach without specifying the trial functions. Hermite trial functions, which were used in the conventional TFEA method, are then introduced in Section 3. Section 4 introduces the procedure to obtain higher order trial functions and provides an alternative procedure for evaluating the weighted residual integrals using quadratures. In Section 5, a Legendre pseudospectral collocation approach is described to study the stability of DDEs. Section 6 provides some notes on the convergence of the spectral element approach and describes its connection to the collocation methods, whereas Section 7 describes the HPM for solving DDEs. Section 8 uses several case studies to compare the efficiency of the new approach in calculating the equilibria solutions and their stability against well-established methods in the literature. Specifically, the stability results are compared with those obtained from the conventional state–space TFEA approach and the Legendre collocation method whereas the equilibria solutions are compared with the numerical simulations and the HPM results. Concluding remarks are then provided in Section 9.

2. TFEA

This section describes the general procedure to ascertain the stability of DDEs using the state–space TFEA method. A scalar, autonomous DDE is used first in Section 2.1 to illustrate the procedure. The approach is then generalized in Section 2.2 to higher order, time-periodic DDEs. To help facilitate the analyses that follow, no specific form is assigned to the trial functions until Sections 3 and 4.1.

TFEA is a discretization technique that can be used to study the stability of autonomous as well as non-autonomous DDEs. The discretization aims to create a dynamic map over a single delay period. The eigenvalues of the map μ can then be used to determine the system stability. More specifically, the system is asymptotically stable if all the eigenvalues are within the unit circle in the complex plane.

2.1. Scalar autonomous DDE

To further explain the procedure, consider the scalar, autonomous DDE described by

$$\dot{x}(t) = \alpha x(t) + \beta x(t-\tau), \tag{1}$$

where α and β are scalars, and τ is a constant time delay. In TFEA, the time-line is discretized into temporal elements as shown in Figure 1. An approximate solution is then sought in each element according to

$$x_j(t) = \sum_{i=1}^{n+1} a_{ji}\phi_i(\eta), \tag{2a}$$

$$x_j(t-\tau) = \sum_{i=1}^{n+1} a_{j-E,i}\phi_i(\eta), \tag{2b}$$

DOI: 10.1002/nme

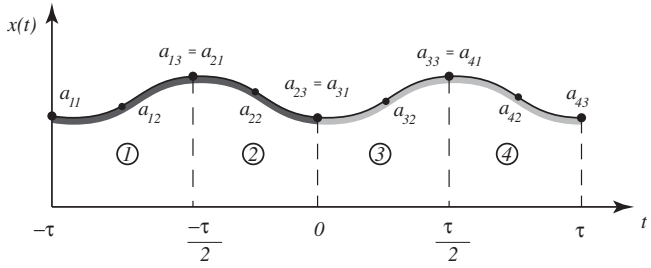

Figure 1. Timeline for the state variable, x, over a time interval of 2τ. Dots denote the locations where the coefficients of the assumed solution are equivalent to the state variable. The beginning and end of each temporal element are marked with dotted lines.

where $\eta=\sigma/t_j$ is the normalization of the local coordinate σ with respect to t_j—the length of the jth element, $n+1$ is the number of the polynomial trial functions $\phi(\eta)$ used, and E is the number of elements in each period. The choice of the trial functions has a great impact on the expandability and robustness of the method as will be shown in the subsequent sections. However, regardless of the trial functions used, the method proceeds by substituting the approximate solution into Equation (1); this gives

$$\sum_{i=1}^{n+1}\left(\frac{1}{t_j}a_{ji}\phi_i'(\eta)-\alpha a_{ji}\phi_i(\eta)-\beta a_{j-E,i}\phi_i(\eta)\right)=\text{error}, \tag{3}$$

where the prime indicates a derivative with respect to η and the error term is associated with the approximation procedure. The error can be minimized by multiplying by a set of test functions and setting the integral over the duration of the element to zero. This is called the method of weighted residuals which also generates enough equations to create the dynamic map. The test functions are required to be independent to obtain a set of linearly independent equations [46]. Further, to keep the resulting matrices square, the number of the test functions is always one less than the number of the trial functions.

Assuming that the index of the test functions $\psi(\eta)$ is p, the weighted expression of Equation (3) becomes

$$\int_0^1\left(\frac{1}{t_j}a_{ji}\phi_i'(\eta)-\alpha a_{ji}\phi_i(\eta)-\beta a_{j-E,i}\phi_i(\eta)\right)\psi_p(\eta)\,\mathrm{d}\eta=0. \tag{4}$$

Applying each test function in turn, the resulting equations for each element can be combined into a global matrix equation. For example, assume that four elements were used to discretize the current and the previous period (illustrated in Figure 1). The resulting expression for the global matrix reads

$$\begin{bmatrix}1&0&0&0&0\\N_{31}^1&N_{32}^1&N_{33}^1&0&0\\N_{31}^2&N_{32}^2&N_{33}^2&0&0\\0&0&N_{41}^1&N_{42}^1&N_{43}^1\\0&0&N_{41}^2&N_{42}^2&N_{43}^2\end{bmatrix}\begin{bmatrix}a_{31}\\a_{32}\\a_{41}\\a_{42}\\a_{43}\end{bmatrix}=\begin{bmatrix}0&0&0&0&1\\P_{11}^1&P_{12}^1&P_{13}^1&0&0\\P_{11}^2&P_{12}^2&P_{13}^2&0&0\\0&0&P_{21}^1&P_{22}^1&P_{23}^1\\0&0&P_{21}^2&P_{22}^2&P_{23}^2\end{bmatrix}\begin{bmatrix}a_{11}\\a_{12}\\a_{21}\\a_{22}\\a_{23}\end{bmatrix}, \tag{5}$$

where the terms inside the matrices of Equation (5) are the following scalar terms:

$$N_{ji}^p=\int_0^1\left(\frac{1}{t_j}\phi_i'(\eta)-\alpha\phi_i(\eta)\right)\psi_p(\eta)\,\mathrm{d}\eta, \tag{6a}$$

$$P_{ji}^p=\int_0^1\beta\phi_i(\eta)\psi_p(\eta)\,\mathrm{d}\eta. \tag{6b}$$

DOI: 10.1002/nme

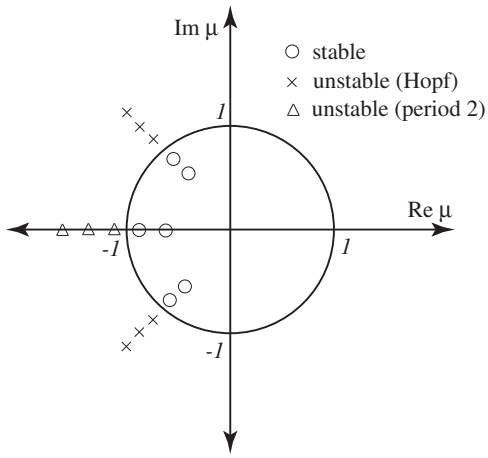

Figure 2. The stability criteria dictate that all the eigenvalues, μ, of the monodromy operator $\mathbf{Q}$, should lie within the unit circle in the complex plane. Moreover, the manner in which the eigenvalues depart the unit circle produces different bifurcation behaviors. For example, an eigenvalue leaving the unit circle through -1 results in a period doubling bifurcation, whereas two complex conjugate eigenvalues departing the unit circle results in secondary Hopf bifurcation.

In Equation (5), it was assumed that three nodes were necessary to interpolate the solution over each element. The trial functions are chosen such that the approximate states of the system are equivalent to the actual states at these nodes. Therefore, the approximation coefficients can be substituted with the actual states at these points, and Equation (5) takes the abbreviated form

$$\mathbf{H}\mathbf{x}_m = \mathbf{G}\mathbf{x}_{m-1}, \tag{7}$$

where m and $m-1$ refer to the current and the previous period, respectively, whereas the terms $\mathbf{H}$ and $\mathbf{G}$ are defined in Equation (5). Equation (7) describes a dynamic map across one delay period of the system in Equation (1). The stability of this system can be determined by the eigenvalues of the monodromy operator $\mathbf{Q}=\mathbf{H}^{-1}\mathbf{G}$. Alternatively, the inversion of $\mathbf{H}^{-1}$ can be avoided by setting the determinant of $\mathbf{G}-\mu\mathbf{H}$ (where μ represents the eigenvalues) to zero. The system is asymptotically stable if all the eigenvalues, or characteristic multipliers of $\mathbf{Q}$, are within the unit circle in the complex plane as shown in Figure 2. Another approach to obtain the dynamic map is a collocation approach which will be explained in Section 5.

2.2. *Generalization to higher order, time-periodic systems*

The state–space TFEA approach presented above can be extended to qth order systems with time-periodic coefficients of the form

$$\dot{\mathbf{x}}(t)=\mathbf{A}(t)\mathbf{x}(t)+\mathbf{B}(t)\mathbf{x}(t-\tau), \tag{8}$$

where $\mathbf{A}(t)=\mathbf{A}(t+T)$ and $\mathbf{B}(t)=\mathbf{B}(t+T)$ are $q\times q$, T-periodic matrices. For simplicity, only the case $T=\tau$, which appears in many applications such as machining processes [47], will be considered here. The extension of TFEA to this class of equations requires more care in the discretization procedure to ensure the time-periodic terms take on the correct values. For example, assume that the time duration of each element is t_j, the discretization then requires the substitution of $t=\sigma+(j-1)t_j=(\eta+j-1)t_j$ into $\mathbf{A}(t)$ and $\mathbf{B}(t)$ to ensure that they assume the correct values over the entire period. In addition, the expression for the current and the delayed state variables is

DOI: 10.1002/nme

written as the vectors

$$\mathbf{x}_j(t) = \sum_{i=1}^{n+1} \mathbf{a}_{ji}\phi_i(\eta), \tag{9a}$$

$$\mathbf{x}_j(t-\tau) = \sum_{i=1}^{n+1} \mathbf{a}_{j-E,i}\phi_i(\eta). \tag{9b}$$

The above approximate expressions are then substituted into Equation (8) and the method of weighted residuals is applied to create a dynamic map—similar to Equation (5). Assuming that each period was discretized with two elements, the resulting global matrices read

$$\begin{bmatrix} \mathbf{I} & \mathbf{0} & \mathbf{0} & \mathbf{0} & \mathbf{0} \\ \mathbf{N}^1_{31} & \mathbf{N}^1_{32} & \mathbf{N}^1_{33} & \mathbf{0} & \mathbf{0} \\ \mathbf{N}^2_{31} & \mathbf{N}^2_{32} & \mathbf{N}^2_{33} & \mathbf{0} & \mathbf{0} \\ \mathbf{0} & \mathbf{0} & \mathbf{N}^1_{41} & \mathbf{N}^1_{42} & \mathbf{N}^1_{43} \\ \mathbf{0} & \mathbf{0} & \mathbf{N}^2_{41} & \mathbf{N}^2_{42} & \mathbf{N}^2_{43} \end{bmatrix} \begin{bmatrix} \mathbf{a}_{31} \\ \mathbf{a}_{32} \\ \mathbf{a}_{41} \\ \mathbf{a}_{42} \\ \mathbf{a}_{43} \end{bmatrix} = \begin{bmatrix} \mathbf{0} & \mathbf{0} & \mathbf{0} & \mathbf{0} & \mathbf{I} \\ \mathbf{P}^1_{11} & \mathbf{P}^1_{12} & \mathbf{P}^1_{13} & \mathbf{0} & \mathbf{0} \\ \mathbf{P}^2_{11} & \mathbf{P}^2_{12} & \mathbf{P}^2_{13} & \mathbf{0} & \mathbf{0} \\ \mathbf{0} & \mathbf{0} & \mathbf{P}^1_{21} & \mathbf{P}^1_{22} & \mathbf{P}^1_{23} \\ \mathbf{0} & \mathbf{0} & \mathbf{P}^2_{21} & \mathbf{P}^2_{22} & \mathbf{P}^2_{23} \end{bmatrix} \begin{bmatrix} \mathbf{a}_{11} \\ \mathbf{a}_{12} \\ \mathbf{a}_{21} \\ \mathbf{a}_{22} \\ \mathbf{a}_{23} \end{bmatrix}, \tag{10}$$

where $\mathbf{I}$ is the $q \times q$ identity matrix. The new expressions for the matrices populating the global matrices are

$$\mathbf{N}^p_{ji} = \int_0^1 \left(\frac{1}{t_j}\mathbf{I}\phi_i'(\eta) - \mathbf{A}((\eta + j - 1)t_j)\phi_i(\eta) \right) \psi_p(\eta)\,\mathrm{d}\eta, \tag{11a}$$

$$\mathbf{P}^p_{ji} = \int_0^1 \mathbf{B}((\eta + j - 1)t_j)\phi_i(\eta)\psi_p(\eta)\,\mathrm{d}\eta, \tag{11b}$$

and they both have the same dimension as $\mathbf{A}(t)$ and $\mathbf{B}(t)$. Equation (10) can be used to define a dynamic map that has the same form as Equation (7). The eigenvalues of the monodromy operator can then be used to determine the stability of the system in Equation (8) with the same stability criterion shown in Figure 2.

Similar to the previous example, the accuracy of the approximation procedure is dependent upon the trial functions. These functions depend on the approximation order—characterized by the number of the interpolation points—as well as the interpolation scheme. The choice of the interpolation points usually includes the end points of the element as well as a set of internal nodes. The inclusion of the end points allows enforcing the continuity conditions across the elements in addition to enforcing the continuity conditions across two periods. In addition to the end points, the order of the approximation is increased by adding more nodes at the middle of the element. These nodes, along with the end points, form a set of distinct points in each element where the approximate states coincide with the actual states. The nodes used to approximate the states are distinct, have a certain distribution, and determine the approximation order. For example, requiring the interpolant to agree with the state variable at the $n+1$ nodes leads to the nth Lagrange polynomial. In contrast, if the interpolant is equivalent to the state variable and its derivative, the resulting trial functions are the $2n+1$ Hermite polynomials. Both of these interpolation schemes are further explained in the sections that follow.

3. HERMITE TRIAL FUNCTIONS

When TFEA was first applied to DDEs in References [42, 45], Hermite polynomials were the trial functions of choice. In that early version, a piecewise approximation of the solution was sought over each temporal element. The assumed solution, as well as its first derivative, had to agree with the exact solution and its first derivative on the interpolation nodes. Therefore, the first version

DOI: 10.1002/nme

of TFEA was limited to at most second-order DDEs, where the coefficients of both the assumed solution and its derivative were interpreted as the displacement and the velocity, respectively, at the interpolation nodes. This requirement on the trial functions naturally led to a Hermite interpolation scheme to generate the necessary polynomials. However, this study will prove that this choice of trial functions is inefficient and that using barycentric Lagrange interpolation leads to a more accurate higher order method.

For instance, let the solution of a second-order DDE over the jth element be $v_j(t)$. Assume that this solution is approximated by a basis of Hermite polynomials on $n+1$ nodes. The resulting expressions for the solution and the delayed argument are

$$\begin{aligned} v_j(t) &= \sum_{i=1}^{n+1} v_j(\eta_i) H_{i0}(\eta) + \sum_{i=1}^{n+1} v'_j(\eta_i) H_{i1}(\eta), \\ v_j(t-\tau) &= \sum_{i=1}^{n+1} v_j(\eta_i - \tau) H_{i0}(\eta) + \sum_{i=1}^{n+1} v'_j(\eta_i - \tau) H_{i1}(\eta). \end{aligned} \tag{12}$$

The Hermite polynomials $H_{i\ell}(\eta)$, where $\ell = 0$ or 1, are constructed to satisfy the property

$$H_{i\ell}^{(s)}(\eta_k) = \delta_{ik}\delta_{s\ell}, \quad s, \ell = 0, 1, \quad i, k = 1, \ldots, n+1, \tag{13}$$

where δ_{ik} and $\delta_{s\ell}$ are the Kronecker deltas, $s = 0$ denotes the undifferentiated Hermite polynomials, whereas $s = 1$ denotes their first derivative with respect to η, and the indices i and k refer to the ith and the kth nodes, respectively. The Hermite polynomials can be obtained using Equation (13) at each node to obtain a system of equations that can be solved for the unknown polynomials' coefficients. Alternatively, the polynomials can be obtained from the corresponding Lagrange polynomials on the $n+1$ nodes as shown in References [48, 49]. Another method to calculate the Hermite polynomials is a Hermite barycentric formula—although this approach is considerably more difficult than its Lagrange counterpart [50, 51].

Upon obtaining the interpolating Hermite polynomials, the original TFEA approach proceeded by substituting the assumed solution into the DDE and used the method of weighted residuals to reduce the approximation error [45]. A dynamic map described by a monodromy operator was then obtained similar to Equation (7). The eigenvalues of the monodromy operator were then used to determine the stability of the DDE using the criteria shown in Figure 2.

The approach was later extended to linear DDEs of arbitrary order expressed in the state–space form [39]. However, for historical reasons, only the Hermite polynomials denoted by $H_{i0}(\eta)$ in Equation (12) were used as trial functions, i.e. $\phi_i(\eta) = H_{i0}(\eta)$, whereas the polynomials $H_{i1}(\eta)$ were ignored. For example, Figure 3 shows the third- and fifth-order Hermite trial functions. The third-order Hermite polynomials are obtained by interpolating at only two nodes—one at the beginning and one at the end of each element—whereas adding an additional interim node leads to a fifth-order Hermite interpolation. To elaborate, if the interpolation nodes are placed at the beginning, middle, and end of each element, the resulting fifth-order Hermite trial functions equivalent to $H_{i0}(\eta)$ are

$$\phi_1(\eta) = 1 - 23\eta^2 + 66\eta^3 - 68\eta^4 + 24\eta^5, \tag{14a}$$

$$\phi_2(\eta) = 16\eta^2 - 32\eta^3 + 16\eta^4, \tag{14b}$$

$$\phi_3(\eta) = 7\eta^2 - 34\eta^3 + 52\eta^4 - 24\eta^5, \tag{14c}$$

while the remaining three polynomials $H_{i1}(\eta)$—where $i = 1, 2, 3$—are ignored. The above trial functions are constructed such that the coefficients of the assumed solution directly represent the state variables at the beginning ($\eta = 0$), middle ($\eta = \frac{1}{2}$), and end ($\eta = 1$) of each temporal element. Figure 1 illustrates that the coefficients of the assumed solution take on the values of the state variables at specific instances in time.

State–space TFEA was successful in the stability studies of a broader class of delay systems such as third-order DDEs [39]. However, the convergence scheme was mostly based on adding

DOI: 10.1002/nme

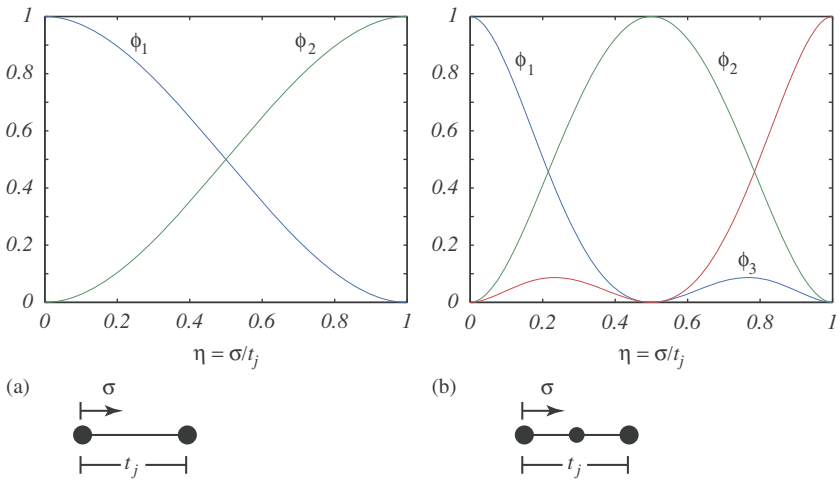

Figure 3. Hermite interpolation polynomials over each element. Graph (a) shows the third-order polynomial interpolated through the beginning and end of the element. Similarly, graph (b) shows the fifth-order polynomial interpolated through the beginning, middle, and end of the element.

more temporal elements, i.e. h-convergence, due to the computational difficulty in increasing the order of the Hermite polynomials and in handling the resulting weighted residual integrals. More specifically, using additional interpolation nodes to improve the approximation comes at the cost of significantly increasing the Hermite interpolant's order. If $n+1$ interpolation nodes are used, then the order of the resulting Hermite polynomials will be $2n+1$. Therefore, it becomes computationally prohibitive to generate and manipulate the resulting trial functions as the approximation order is increased to higher values. The restriction on the order of the trial functions prevents taking full advantage of spectral convergence rates, i.e. p-convergence, and forces an h-convergence scheme.

4. HIGHER ORDER TRIAL FUNCTIONS—SPECTRAL ELEMENTS

To increase the order of approximation, it is essential to choose the location of the interpolation nodes such that a well-conditioned polynomial approximation is obtained. More specifically, except for low values of n, equidistant nodes lead to highly ill-conditioned systems and give rise to the Runge phenomenon [52]. A better approach is to use a set of asymptotically arcsin-distributed nodes such as the Legendre–Gauss–Lobatto (LGL) points [53]. These sets of nodes are more clustered at the end of the elements with an asymptotic density proportional to $(1-u^2)^{-1/2}$ as $n\to\infty$ [52]. More specifically, the $n+1$ LGL points are the roots of the polynomial $(1-u^2)L'_n(u)$ where u ranges from -1 to 1 and $L_n(u)$ is the Legendre polynomial of order n [54]. These points can be shifted to an arbitrary interval $[a,b]$ through the relation

$$\tilde{u}=\frac{b-a}{2}u+\frac{b+a}{2}, \tag{15}$$

where $u\in[-1,1]$ and $\tilde{u}\in[a,b]$, e.g. if $a=0$ and $b=1$, then $\eta=\tilde{u}$.

Having selected an appropriate set of nodes, the higher-order trial functions can be obtained through Lagrange interpolation. In contrast to a Hermite interpolation scheme, the approximate function is required to agree with the actual one at the interpolation nodes whereas the derivative information is not used. This helps in obtaining higher-order trial functions while maintaining manageable polynomials. For example, if $n+1$ LGL points are used, a Hermite interpolation scheme would result in polynomials of order $2n+1$ compared with n for a Lagrange scheme.

DOI: 10.1002/nme

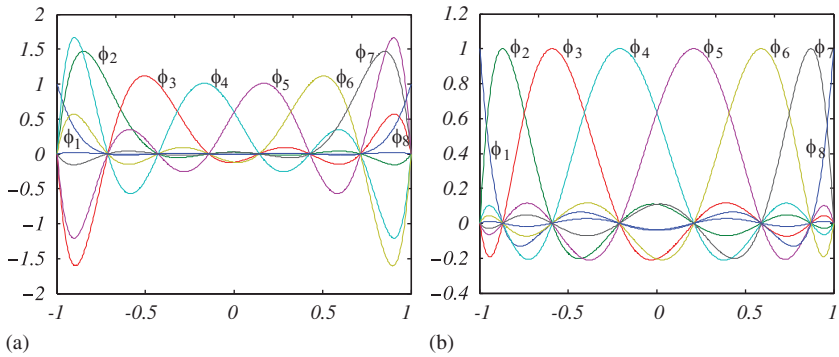

Figure 4. Lagrange trial functions of order 7 obtained through interpolating 8 points through an element with (a) equidistant nodes and (b) through the LGL points.

Using the Lagrange formula, the trial functions can be obtained according to

$$\phi_i(\eta)=\frac{\prod_{k=1,k\neq i}^{n+1}(\eta-\eta_k)}{\prod_{k=1,k\neq i}^{n+1}(\eta_i-\eta_k)}, \tag{16}$$

where the indices i and k refer to the ith and kth interpolation nodes, respectively. The Lagrange polynomial ϕ_i corresponding to the ith node has the property

$$\phi_i(\eta_k)=\begin{cases}1, & i=k,\\ 0 & \text{otherwise,}\end{cases} \qquad j,k=1,\ldots,n+1. \tag{17}$$

Figure 4 shows the resulting seventh-order trial functions using eight nodes that are equally spaced in graph (a) while the LGL distribution is used in graph (b). These plots are generated over the range $[-1,1]$, and they match those in Reference [54].

Equation (16) comes from the typical form of Lagrange interpolation which is only recommended for a small number of nodes. Specifically, using this equation with high values for n requires a high number of additions and multiplications and yields the computation numerically unstable [52]. In agreement with Reference [55], a more effective representation of Lagrange polynomials is provided by the barycentric formula according to

$$\phi_i(\eta)=\frac{\dfrac{\varpi_i}{\eta-\eta_i}}{\sum_{k=1}^{n+1}\dfrac{\varpi_k}{\eta-\eta_k}}, \tag{18}$$

where ϖ_k are the barycentric weights given by

$$\varpi_k=\frac{1}{\prod_{k\neq j}(\eta_j-\eta_k)}, \qquad j=1,\ldots,n+1. \tag{19}$$

The barycentric formula requires less computational effort and has better numerical stability than the conventional Lagrange representation [52, 55]; therefore, it was used to generate the trial functions in the present study.

In addition to being a more efficient tool to generate the trial functions, the barycentric weights can be used to obtain the value of the derivative of the trial functions evaluated at the interpolation

DOI: 10.1002/nme

nodes according to

$$\phi_i'(\eta_k)=\begin{cases}\dfrac{\varpi_i/\varpi_k}{\eta_i-\eta_k}, & i\neq k\\ \displaystyle\sum_{i=0,i\neq k}^{n+1}\dfrac{-\varpi_i/\varpi_k}{\eta_i-\eta_k}, & i=k\end{cases} \tag{20}$$

These values are useful in evaluating the weighted residual integrals of Equations (6) and (11) using an LGL quadrature as will be shown in Section 4.1. Moreover, the values defined in Equation (20) form the entries of the differentiation matrix which describes a linear transformation from the values of the trial functions at the nodes to the values of the derivative of the trial functions at the same nodes. For example, assume that the vector $\mathbf{z}$ contains the values of a function $g(t)$ evaluated at the $n+1$ LGL points. If the vector $\mathbf{z}'$ contains the derivative of g evaluated at the same collocation points, then the effect of differentiating the function at these points can be described by a differentiation matrix $\mathbf{D}$ according to

$$\mathbf{z}'=\mathbf{D}\mathbf{z}, \tag{21}$$

where the entries of $\mathbf{D}$ are defined from Equation (20) according to

$$D_{ki}=\phi_i'(\eta_k). \tag{22}$$

One of the most important applications of differentiation matrices is in spectral collocation methods for the numerical solutions of differential equations. An example of a collocation technique for obtaining the stability of DDEs using LGL nodes will be described in Section 5.

4.1. LGL quadrature

In the conventional TFEA approach, the weighted residual integrals were evaluated analytically using a software with symbolic manipulation capability. This limited the conventional approach to systems where such analytical expressions can be obtained. In contrast, another advantage of using the LGL points in the current study is that evaluating the integrals using a Gauss quadrature becomes straightforward since the quadrature points are already calculated when the trial functions are obtained. Applying a quadrature rule, as opposed to analytical manipulations, allows faster and more robust calculations of the involved integrals. To increase the order of an element by one, another internal node needs to be added. The trial functions and the associating integrals can then be calculated accordingly. This allows increasing the order of the approximation until a convergent solution is obtained, a procedure that is commonly referred to as the spectral element approach.

The LGL quadrature gives the best estimate of an integral through replacing it by a weighted summation of the function values at the LGL points. These points are identical to the ones used in this section to generate higher-order trial functions. Denoting the integrand resulting from the weighted residual method by $f(\eta)$, the corresponding expression for the LGL quadrature reads

$$\int_0^1 f(\eta)\,\mathrm{d}\eta\approx\sum_{k=1}^{n+1}w_k f(\eta_k), \tag{23}$$

where η_k are the Legendre points shifted from the interval $[-1,1]$ to $[0,1]$ using Equation (15), $f(\eta_k)$ are the values of $f(\eta)$ evaluated at the LGL points [56], and w_k are the LGL quadrature weights given by the equation

$$w_k=\begin{cases}\dfrac{2}{n(n+1)}, & k=1,n+1\\ \dfrac{2}{n(n+1)(L_n(\eta_k))^2} & \text{otherwise,}\end{cases} \tag{24}$$

If $f(\eta)$ is a polynomial with a degree of at most $2n+1$, then it is sufficient to use $n+1$ points in the Gauss quadrature to yield an accurate estimate of the integral [57]. Equations (23) and (24)

DOI: 10.1002/nme

can be used to evaluate the integrals in Equations (6) and (11) which can then be used to populate the corresponding global matrices. For example, consider the general case of the weighted residual integrals in Equation (11). Applying the LGL quadrature rule to these integrals yields

$$\mathbf{N}_{ji}^{p} = \sum_{k=1}^{n+1} \left(\frac{1}{t_j} \mathbf{I} \phi_i'(\eta_k) \psi_p(\eta_k) w_k \right) - \sum_{k=1}^{n+1} \left(\mathbf{A}((\eta_k + j - 1)t_j) \phi_i(\eta_k) \psi_p(\eta_k) w_k \right), \tag{25a}$$

$$\mathbf{P}_{ji}^{p} = \sum_{k=1}^{n+1} \left(\mathbf{B}((\eta_k + j - 1)t_j) \phi_i(\eta_k) \psi_p(\eta_k) w_k \right). \tag{25b}$$

However, recall the property of $\phi_i(\eta_k)$ given in Equation (17) which can be restated as $\phi_i(\eta_k) = \delta_{ik}$, where δ_{ik} is the Kronecker delta. Consequently, the terms of the series multiplying $\phi_i(\eta_k)$ vanish except when $i = k$ in which case $\phi_i(\eta_i) = 1$. This property can be used to simplify the above expressions to obtain

$$\mathbf{N}_{ji}^{p} = \sum_{k=1}^{n+1} \left(\frac{1}{t_j} \mathbf{I} \phi_i'(\eta_k) \psi_p(\eta_k) w_k \right) - \mathbf{A}((\eta_i + j - 1)t_j) \psi_p(\eta_i) w_i, \tag{26a}$$

$$\mathbf{P}_{ji}^{p} = \mathbf{B}((\eta_i + j - 1)t_j) \psi_p(\eta_i) w_i. \tag{26b}$$

Equation (26) shows the advantage of using a quadrature rule, as opposed to analytical calculations, to evaluate the weighted residual integrals; in addition to handling more complex integrals, the evaluation of these integrals is reduced to a weighted summation of matrices. Furthermore, choosing the quadrature points to be identical to the interpolation points allows the property of Equation (17) to simplify the quadrature even further. These features yield a spectral element method that does not require obtaining the expressions of the trial functions, only the barycentric weights associated with them. These weights can be obtained only by knowing the set of interpolation points within each element. In other words, with the current approach it becomes possible to evaluate the weighted residual integrals using only the information from the temporal mesh and the state–space matrices.

5. LEGENDRE COLLOCATION APPROACH

The TFEA approach expands the approximate states as a linear combination of interpolating polynomials with unknown coefficients. Using the method of weighted residuals, a sufficient number of equations is obtained to create a dynamic map. This section presents an alternative procedure to generate the necessary equations through a Legendre collocation approach. Although a similar approach using Chebyshev points has been used in References [2, 58, 59], this study will use LGL points to give a better comparison with the method described in the previous sections.

The approximate solution is still given by Equation (2) and the interpolation points are still the LGL nodes. However, instead of using the weighted residual method to reduce the approximation error, the system is evaluated at the $N+1$ collocation points to generate the necessary number of equations. Another major difference is that the derivative on the collocation points can be determined in terms of the function values at these points. In general, these values can be obtained from Equations (20) and (22), and they form the entries of the spectral differentiation matrix $\mathbf{D}$. However, using the LGL nodes gives a simplified expression for the entries of $\mathbf{D}$ defined on $[-1, 1]$. Specifically, the dimension of this matrix is $(N+1) \times (N+1)$ and its entries are given by [60]

$$D_{00} = -D_{NN} = -\frac{N(N+1)}{4}, \tag{27a}$$

$$D_{km} = \begin{cases} \dfrac{L_N(t_k)}{L_N(t_m)} \dfrac{1}{(t_k - t_m)}, & k \neq m, \\ 0 & \text{otherwise.} \end{cases} \tag{27b}$$

DOI: 10.1002/nme

To obtain the differentiation matrix entries for the interval $[a,b]$, the entries defined in Equation (27) are multiplied by the scaling factor $2/(b-a)$.

The Legendre collocation approach can be used to determine the stability of delay systems written in state–space form such as Equation (8). In this case, the equation is evaluated at the $N+1$ collocation points which gives

$$\hat{\mathbf{D}}\mathbf{x}_m = \hat{\mathbf{M}}_A\mathbf{x}_m + \hat{\mathbf{M}}_B\mathbf{x}_{m-1}, \tag{28}$$

where $\mathbf{x}_m$ contains the values of $\mathbf{y}(t)$ in the interval $t\in[0,\tau]$ while $\mathbf{x}_{m-1}$ contains the values of the initial function $\varphi(t)=\mathbf{y}(t-\tau)$ in $t\in[-\tau,0]$ according to

$$\mathbf{x}_m = \begin{bmatrix} \mathbf{y}(t_0) \\ \mathbf{y}(t_1) \\ \vdots \\ \mathbf{y}(t_N) \end{bmatrix}, \quad \mathbf{x}_{m-1} = \begin{bmatrix} \boldsymbol{\varphi}(t_0) \\ \boldsymbol{\varphi}(t_1) \\ \vdots \\ \boldsymbol{\varphi}(t_N) \end{bmatrix}. \tag{29}$$

In order to describe the matrix $\hat{\mathbf{D}}$, the $q(N+1)$ square differential operator $\mathbb{D}$ is defined first as the Kronecker product $\mathbb{D}=\mathbf{D}\otimes\mathbf{I}_q$, where $\mathbf{D}$ was defined in Equation (27) and $\mathbf{I}_q$ is an identity matrix. The matrix $\hat{\mathbf{D}}$ is then a modified version of the spectral differentiation matrix $\mathbb{D}$ with the following changes (1) multiplying by $2/\tau$ to account for the shift $[-1,1]\to[0,\tau]$, and (2) changing the last q rows to $[\mathbf{0}_q\mathbf{0}_q\ldots\mathbf{I}_q]$ where $\mathbf{0}_q$ and $\mathbf{I}_q$ are $q\times q$ null and identity matrices, respectively. The change in the last q rows of $\hat{\mathbf{D}}$, (and the last q rows of $\hat{\mathbf{M}}_A$ and $\hat{\mathbf{M}}_B$ as will be shown shortly), is necessary to enforce the continuity condition which, for this particular case, implies that the states are equal at the end of one period and the beginning of the subsequent one.

The $q(N+1)$ square matrix $\hat{\mathbf{M}}_A$ has the entries

$$\hat{\mathbf{M}}_A = \begin{bmatrix} \mathbf{A}(t_0) & & & & \\ & \mathbf{A}(t_1) & & & \\ & & \ddots & & \\ & & & \mathbf{A}(t_{N-1}) & \\ \mathbf{0}_q & \mathbf{0}_q & \ldots & \mathbf{0}_q & \mathbf{0}_q \end{bmatrix}, \tag{30}$$

where $\mathbf{A}(t_i)$ is the value of $A(t)$ in Equation (8) evaluated at the ith collocation point. Similarly, the square $q(N+1)$ matrix, $\hat{\mathbf{M}}_B$, has the entries

$$\hat{\mathbf{M}}_B = \begin{bmatrix} \mathbf{B}(t_0) & & & & \\ & \mathbf{B}(t_1) & & & \\ & & \ddots & & \\ & & & \mathbf{B}(t_{N-1}) & \\ \mathbf{I}_q & \mathbf{0}_q & \ldots & \mathbf{0}_q & \mathbf{0}_q \end{bmatrix}, \tag{31}$$

where $\mathbf{B}(t_i)$ is the value of $B(t)$ in Equation (8) evaluated at the ith collocation point.

Equation (28) can be rearranged to obtain the dynamic map

$$\mathbf{x}_m = \mathbf{Q}\mathbf{x}_{m-1}, \tag{32}$$

where the stability is determined by the eigenvalues of $\mathbf{Q}$ as was shown in Figure 2.

DOI: 10.1002/nme

6. CONNECTION BETWEEN COLLOCATION AND SPECTRAL ELEMENT

TFEA and collocation methods differ mainly in the approach they each use to reduce the approximation error, see Equation (3). However, although collocation methods and TFEA may seem different, they are actually closely related [40]. The connection between the two methods can be revealed by considering the weighted residual integral

$$\int_0^1 \left(\frac{1}{t_j}a_{ji}\phi_i'(\eta)-\alpha a_{ji}\phi_i(\eta)-\beta a_{j-E,i}\phi_i(\eta)\right)\psi_p(\eta)\,\mathrm{d}\eta=0. \tag{33}$$

which was introduced in Equation (4). Recall that the collocation methods are global approximation techniques whereas TFEA employs piecewise approximation on a number of elements. However, if the number of elements is set to 1, then TFEA and collocation become defined on the same domain and the length of the element becomes the system period $t_j=T$. Making this assumption in Equation (4), the key difference between the collocation and TFEA methods becomes the choice of the test functions $\psi_p(\eta)$.

These test functions are introduced to reduce the error associated with the approximation as well as to generate enough equations to construct a dynamic map. Since TFEA and collocation methods adopt different strategies to reduce the error, the test functions used in Equation (4) define the resulting analysis technique. Traditionally, there are three common choices for the set of test functions [40, 46]:

$$\{\psi_p(\eta)\}_{p=1}^n=\{\delta(\eta-\eta_p)\}_{p=1}^n \quad \text{(Collocation)}, \tag{34a}$$

$$\{\psi_p(\eta)\}_{p=1}^n\subset\{\phi_i(\eta)\}_{i=1}^{n+1} \quad \text{(TFEA, Galerkin)}, \tag{34b}$$

$$\psi_p(\eta)\in\{\phi_i(\eta)\}_{i=1}^{n+1} \quad \text{for all } p \text{ (TFEA, Petrov–Galerkin)} \tag{34c}$$

where $\{\eta_p\}$ is a suitable set of collocation points and $\delta(\eta-\eta_p)$ is the Dirac delta function. Equation (34a) reveals that collocation methods are special cases of the weighted residual approach caused by using Dirac delta test functions.

Analogously, using a Gaussian quadrature rule to evaluate the integral in Equation (33) shows the transformation from a collocation method to TFEA. Specifically, assume $E=1$ and that the quadrature points coincide with the interpolation points. The resulting expressions for one element are shown in Equation (26) and they can be rewritten for all the interpolation points within the element as

$$\begin{bmatrix}[\mathbf{W}_{\mathrm{res}}(\mathbf{D}\otimes\mathbf{I}_q-\mathbf{M}_A)]\\ \begin{bmatrix}\mathbf{I}_q & \mathbf{0} & \dots & \mathbf{0}\end{bmatrix}\end{bmatrix}\begin{bmatrix}\mathbf{x}_0\\ \mathbf{x}_1\\ \vdots\\ \mathbf{x}_n\end{bmatrix}_m=\begin{bmatrix}[\mathbf{W}_{\mathrm{res}}]\\ [\mathbf{0} & \dots & \mathbf{0} & \mathbf{I}_q]\end{bmatrix}\begin{bmatrix}\mathbf{x}_0\\ \mathbf{x}_1\\ \vdots\\ \mathbf{x}_n\end{bmatrix}_{m-1} \tag{35}$$

where the entries of the $(n+1)\times(n+1)$ differentiation matrix $\mathbf{D}$ are given by Equation (22) and the last q rows are added to enforce the continuity condition at $t=0$. The diagonals of the $(n+1)$ square matrices $\mathbf{M}_A$ and $\mathbf{M}_B$ contain, respectively, the matrices $\mathbf{A}(t)$ and $\mathbf{B}(t)$ from Equation (8) evaluated at the $n+1$ collocation points. The matrices $\mathbf{I}_q$ and $\mathbf{0}_q$ are the $q\times q$ identity and zero matrices, respectively, whereas the $qn\times q(n+1)$ transformation matrix W_{res} is given by

$$\mathbf{W}_{\mathrm{res}}=\left(\begin{bmatrix}w_0 & w_1 & \dots & w_n\\ w_0 & w_1 & \dots & w_n\\ \vdots & & & \vdots\\ w_0 & w_1 & \dots & w_n\end{bmatrix}\circledast\begin{bmatrix}\psi_0(t_0) & \dots & \psi_0(t_n)\\ \psi_1(t_0) & \dots & \psi_1(t_n)\\ \vdots & & \vdots\\ \psi_{n-1}(t_0) & \dots & \psi_{n-1}(t_n)\end{bmatrix}\right)\otimes\mathbf{I}_q \tag{36}$$

DOI: 10.1002/nme

where w_k are the interpolation weights given by Equation (24) while the symbol $\circledast$ denotes element-wise multiplication. Equation (35) is equivalent to the abbreviated form $\mathbf{H}\mathbf{x}_m = \mathbf{G}\mathbf{x}_{m-1}$ presented in Equation (7). Note that although the resulting matrices for $E=1$ are full, for $E>1$ they are not. Nevertheless, the transformation in Equation (35) can be expanded to the case of multiple elements.

To elaborate, the expression for $\mathbf{H}$ when E elements are used each with $n+1$ discretization points becomes

$$\mathbf{H} = \begin{bmatrix} [\hat{\mathbf{W}}_{\text{res}}(\mathbf{D}_1 \otimes \mathbf{I}_q - \mathbf{M}_A^{e=1})] & & & & & & \\ & [\hat{\mathbf{W}}_{\text{res}}(\mathbf{D}_2 \otimes \mathbf{I}_q - \mathbf{M}_A^{e=2})] & & & & & \\ & & \ddots & & & & \\ & & & [\hat{\mathbf{W}}_{\text{res}}(\mathbf{D}_j \otimes \mathbf{I}_q - \mathbf{M}_A^{e=j})] & & & \\ & & & & \ddots & & \\ & & & & & [\hat{\mathbf{W}}_{\text{res}}(\mathbf{D}_E \otimes \mathbf{I}_q - \mathbf{M}_A^{e=E})] & \\ \mathbf{0}_q & \mathbf{0}_q & \cdots & \cdots & \mathbf{0}_q & \mathbf{0}_q & \mathbf{I}_q \end{bmatrix}, \tag{37}$$

where $\hat{\mathbf{W}}_{\text{res}} = \mathbf{W}_{\text{res}} \otimes \mathbf{I}_q$, $\mathbf{D}_j$ is the $(n+1)\times(n+1)$ differentiation matrix on the jth element while the $q(n+1)$ block diagonal matrix $\mathbf{M}_A^{e=j}$ contains the values of $\mathbf{A}(t)$ at the $n+1$ collocation points within the jth element. All the non-labeled entries of $\mathbf{H}$ in Equation (37) are zeros and the resulting structure is a block matrix with any two blocks overlapping only horizontally by q columns. For a large number of elements, most of the entries in $\mathbf{H}$ become zeros; hence, the resulting sparse structure can be exploited to speed up stability computations via sparse matrix eigenvalue solvers [61]. Similarly, the expression for the $\mathbf{G}$ matrix can be obtained using the matrices $\mathbf{W}_{\text{res}}$, $\mathbf{B}(t)$ and the last q rows of Equation (35) to enforce continuity at $t=0$.

Equations (35) and (37) suggest that the spectral element approach we present here can be thought of as a linear transformation of collocation methods. Collocation methods are well documented in the literature and a proof of their convergence can be found in Reference [36]. Further, the entries of the transformation matrix $\mathbf{W}_{\text{res}}$ are constituted from continuous independent test functions and Gaussian quadrature weights. Since linear transformations are well behaved with respect to continuity and convergence, the application of this matrix preserves the convergence properties as evidenced by the various computational studies using TFEA found in the literature as well as the examples we used in this study [3, 42, 45, 62].

7. SOLUTIONS TO DDES USING HPM

The HPM is a modern analytical technique that couples homotopy and perturbation theory [18–21]. It is characterized by a quickly converging series and the elimination of the 'small parameter' assumption—the major limitation in typical perturbation methods [19, 30]. To illustrate the basic steps in HPM, consider the following general DDE:

$$\mathscr{L}(x(t)) + \mathscr{A}(x(t-\tau), f(t)) = 0, \quad x \in \mathbb{R} \tag{38a}$$

$$x(s) = \Theta \quad \text{for } s \in [-\tau, 0] \tag{38b}$$

where the time delay τ is a positive scalar, $f(t)$ is a known analytic function and the initial function Θ is continuous on $[-\tau, 0]$. The operator $\mathscr{L}$ is a linear differential operator while $\mathscr{A}$ contains the delayed arguments as well as any other time-dependent functions. Note that there is some degree of freedom in selecting the linear part $\mathscr{L}$. However, the solution of this part strongly influences the overall approximate solution; therefore, $\mathscr{L}$ has to be carefully chosen to ensure that the resulting linear part is stable, see Reference [63] for more details.

DOI: 10.1002/nme

We construct a homotopy $\mathscr{H}(\rho, v):[0,1]\times\mathbb{R}\to\mathbb{R}$ on Equation (38) that satisfies

$$\mathscr{H}(\rho, v)=(1-\rho)[\mathscr{L}(v(t))-\mathscr{L}(x_0(t))]+\rho[\mathscr{L}(v(t))+\mathscr{A}(v(t-\tau), f(t))] \tag{39}$$

$$=\mathscr{L}(v(t))-\mathscr{L}(x_0(t))+\rho\mathscr{L}(x_0(t))+\rho[\mathscr{A}(v(t-\tau), f(t))]=0, \tag{40}$$

where $\rho\in[0,1]$ is an embedding parameter while $x_0(t)$ is an initial approximation, or guess, of Equation (38) which satisfies the initial conditions. The initial guess x_0 can be assigned freely [18]; however, a good initial approximation can accelerate convergence [28].

Obviously, Equation (39) yields a linear ordinary differential equation when $\rho=0$ whereas a value of $\rho=1$ gives back the original DDE according to

$$\mathscr{H}(0, v)=\mathscr{L}(v(t))-\mathscr{L}(x_0(t))=0 \tag{41a}$$

$$\mathscr{H}(1, v)=\mathscr{L}(v(t))+\mathscr{A}(v(t-\tau), f(t))=0. \tag{41b}$$

Therefore, changing the homotopy parameter ρ from 0 to 1 is equivalent to changing $v(\rho, t)$ from $x_0(t)$ to $x(t)$—a process called deformation in topology. Since $0\leqslant\rho\leqslant1$, the embedding parameter ρ can be considered a small parameter. Hence, the solution of Equation (39) can be written as a power series in ρ according to

$$v=v_0+\rho v_1+\rho^2 v_2+\cdots \tag{42}$$

Substituting Equations (42) into (39) and separating the resultant expression into powers of ρ produce an infinite number of differential equations in v. These equations can be successively solved up to the desired expansion order in ρ, usually less than 4, to obtain v in Equation (42). The initial conditions necessary for solving the differential equations can typically be chosen according to

$$\frac{\mathrm{d}^j v_i(0)}{\mathrm{d}^j t}=\begin{cases}\dfrac{\mathrm{d}^j x(0)}{\mathrm{d}^j t} & \text{if } i=0,\\ 0 & \text{if } i>0,\end{cases} \tag{43}$$

where $\mathrm{d}^0 v/\mathrm{d}t^0=v$. The approximate solution is then obtained by setting the homotopy parameter ρ to 1 according to

$$x(t)\approx\lim_{\rho\to1} v=v_0+v_1+v_2+\cdots \tag{44}$$

The symbolic capabilities of modern computer software can be used to quickly and accurately obtain the expression of the approximate solution. Note that for some problems with complicated time-dependent coefficients no analytical expressions can be computed. Nevertheless, HPM can still be used to obtain a set of simpler equations whose numerical solution is easier than the original equation. In the current study we used Mathematica to obtain the necessary expressions and/or the necessary numerical solutions.

8. CASE STUDIES

This section compares the spectral element method to each of the conventional state–space TFEA, the Legendre collocation approach and HPM using three case studies. In each case, the approximation errors for both the maximum Floquet multiplier and the equilibria solutions are given.

For stability comparisons, the conventional TFEA approach uses the fifth-order Hermite polynomials described in Equation (14) and relies on an h-convergence scheme. Whereas to emphasize the p-convergence capability of the spectral element approach, the number of elements is fixed to 1 and the order of the trial functions n is increased. For the Legendre collocation method, the number of collocation points N is increased to obtain spectral convergence. The hp-convergence of the spectral element method is then shown in a series of plots where the order of the trial functions is held fixed while the number of elements is varied. In each example, the stability diagram to

DOI: 10.1002/nme

which all the methods converged is shown and the error associated with calculating the maximum Floquet multiplier is given.

A comparison between the equilibria solutions obtained through the spectral element approach, HPM, and numerical simulations is also provided. Since in most practical situations the exact solutions cannot be obtained, the numerical simulations obtained using Mathematica's NDSolve are treated as the exact solutions. Error norms are calculated on the mesh points of the spectral element method using various combinations of E and n. The results are then compared with the corresponding HPM error norms obtained using the first and second approximation orders.

The error norms that will be used in this section are first described in Section 8.1. The first example in Section 8.2 is the scalar autonomous DDE of Equation (1). Section 8.3 studies an autonomous third-order DDE whereas Section 8.4 investigates the equations of an unbalanced rotating shaft with feedback gain; which is described by coupled second-order DDEs with time-periodic coefficients.

8.1. Error analysis

For stability comparisons, the error measure used is the absolute error

$$\varepsilon_{\text{stability}} = |\lambda - \mu*|, \tag{45}$$

where $\lambda = \max|\mu|$ is an approximation of the maximum eigenvalue, whereas $\mu*$ is the reference maximum eigenvalue obtained with high-order Legendre collocation approach, i.e. $\mu* = \max(|\mu(N_{\max}|))$. In this study, the number of the collocation points was chosen to be $N_{\max} = 40$.

On the other hand, the measures that we use here to compare the approximate solutions obtained with the spectral element method and HPM are the two error norms

$$\varepsilon_2 = \frac{\|x - x_{\text{ref}}\|_2}{\|x_{\text{ref}}\|_2}, \tag{46a}$$

$$\varepsilon_\infty = \frac{\|x - x_{\text{ref}}\|_\infty}{\|x_{\text{ref}}\|_\infty}, \tag{46b}$$

where x is the approximate solution while x_{ref} is the reference solution obtained from simulation. The discrete norms ℓ_2 and ℓ_∞ are defined according to

$$\|z\|_2 = \left(\sum_{k=1}^{n+1} (z_k)^2\right)^{\frac{1}{2}} \quad (\ell_2 \text{ discrete norm}), \tag{47a}$$

$$\|z\|_\infty = \max_k |z_k| \quad (\ell_\infty \text{ discrete norm}). \tag{47b}$$

The error norms defined in Equation (46) are calculated on the mesh generated with the spectral element approach.

8.2. Scalar example

Consider the scalar DDE described by:

$$\dot{x}(t) = \alpha x(t) + \beta x(t - \tau), \tag{48a}$$

$$x(s) = 0.1\mathrm{e}^{-0.8t} \quad \text{for } s \in [-\tau, 0]. \tag{48b}$$

This equation has been widely used to investigate the effect of delays on the solutions and bifurcations of DDEs [64–66]. If the scalars α and β are chosen as the control parameters and $\tau = 1$, then the stability of the system in the control parameter space can be described by the stability diagram in Figure 5(a).

Figure 5(b) shows the absolute difference $|\lambda - \mu*|$ at the (α, β) point $(-1, 0.0754)$ for the different methods. The integers on the horizontal axis represent the following: (1) the number of

DOI: 10.1002/nme

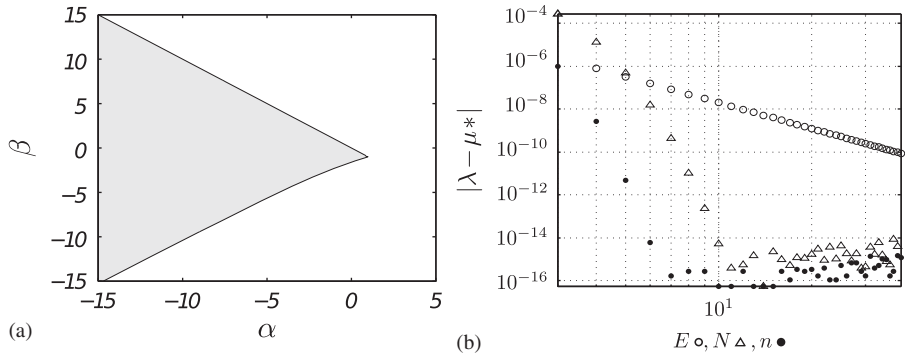

Figure 5. The stability diagram for Equation (1) and the spectral convergence plots for the (α, β) point $(-1, 0.0754)$. In graph (a) the stable regions are shaded whereas the unstable regions are left unshaded. Graph (b) shows the convergence of the maximum eigenvalue as a function of: (1) the number of elements in the conventional TFEA approach (circles), (2) the number of collocation points in the Legendre collocation method (triangles), and (3) the order of the Lagrange trial functions (dots).

Table I. The relative errors associated with using different approximation orders of HPM to solve Equation (1).

HPM order	ε_2	ε_∞
0	1.39651×10^{-2}	1.3111×10^{-2}
1	7.49933×10^{-8}	1.07204×10^{-7}
2	1.67387×10^{-3}	1.41363×10^{-3}

elements for the conventional TFEA approach (circles), (2) the number of the collocation points for the Legendre collocation approach (triangles), and (3) the order of the Lagrange polynomial in the spectral element method (dots). It can be seen that the conventional TFEA approach follows a linear convergence scheme whereas both spectral element and the collocation method demonstrate exponential (or spectral) convergence. In addition, the spectral element method converges faster than the collocation approach.

The *hp* refinement capability of the spectral element approach is shown in Figure 7. Figure 7(a) corresponds to the error associated with calculating the maximum Floquet multiplier in Equation (48). In each curve, the order of the trial functions was held constant while the number of elements was varied between 1 and 24. It can be seen that a convergent solution can be obtained by either increasing the order of the trial functions or the number of elements. Moreover, it can be seen that increasing both E and n leads to faster convergence.

To obtain the equilibria solutions of Equation (48) using HPM, the steps described in Section 7 yield a set of equations that correspond to different powers of ρ according to

$$\rho^0 : \dot{v}_0 - \dot{x}_0 - \alpha(v_0 - x_0) = 0 \quad \text{where } v_0(0) = x(0) = 0.1 \tag{49}$$

$$\rho^1 : \dot{v}_1 + \dot{x}_0 - \alpha(v_1 + x_0) - \beta v_0(t-\tau) = 0 \quad \text{where } v_1(0) = 0 \tag{50}$$

$$\rho^k : \dot{v}_k - \alpha v_k - \beta v_{k-1}(t-\tau) = 0 \quad \text{where } v_k(0) = 0 \quad \text{for } k \geqslant 2 \tag{51}$$

where the initial solution $x_0(t) = 0.1\mathrm{e}^{-0.8t}$ was used. The equilibria solution obtained with a second-order HPM is plotted with a dashed line in Figure 9(a) along with the simulated solution (solid line) and the spectral element solution (x). In generating the spectral element solution, the parameters $E = 3$ and $n = 6$ were used. It can be seen that both HPM and the spectral element approach show good agreement with numerical simulations.

A quantitative measure of the quality of the solutions obtained with the spectral element approach and HPM is shown in Figure 10 and Table I, respectively. Figures 10(a) and (b) show the errors calculated using Equation (46) with the spectral element method. In each curve, the number of

DOI: 10.1002/nme

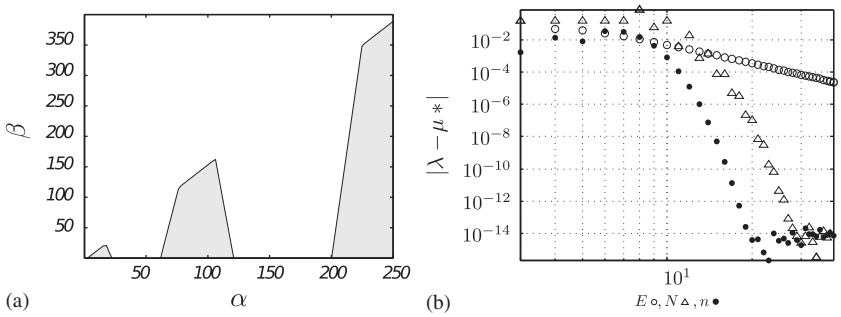

Figure 6. The stability diagram for Equation (52) and the spectral convergence plots for the (α, β) point $(202.04, 28.38)$. In graph (a), the stable regions are shaded whereas the unstable regions are left unshaded. Graph (b) shows the convergence of the maximum eigenvalue as a function of: (1) the number of elements in the conventional TFEA approach (circles), (2) the number of collocation points in the Legendre collocation method (triangles), and (3) the order of the Lagrange trial functions (dots).

elements was held constant while the order of the trial functions was varied between 2 and 40. It can be seen that for this simple example the approximate solution converged quickly to the reference solution and round off errors dominated as n was increased.

The errors associated with using HPM up to the second-order approximation are shown in Table I. The discrete errors were calculated using the mesh points of the spectral element approach with $E=3$ and $n=40$. It can be seen that although good results are obtained using only the first-order approximation, the quality of the solution deteriorates when the order is increased to 2. In contrast, the spectral element approach showed a remarkable accuracy compared with numerical simulations as shown in Figures 10(a)–(b).

8.3. Third-order example

Consider the following third-order delay equation:

$$\frac{\mathrm{d}^3 y}{\mathrm{d}t^3} + \alpha \dot{y} + \beta y(t-\tau) = 0, \tag{52a}$$

$$y(s) = 10\mathrm{e}^{-0.16t} \quad \text{for } s \in [-\tau, 0]. \tag{52b}$$

with a delay value of $\tau=1$ and control parameters α and β. Equation (52) is the delayed linearized version of the so-called Jerk equation [67]. This equation appears, for example, when studying the oscillations of non-linear vacuum tube circuits [68]. In addition, Equation (52) appears when certain second-order DDEs with distributed delays are transformed to a higher order system with only discrete delays, e.g. when modeling cutting forces in turning via a distributed force model [44].

Note that determining the stability of a third-order DDE would not have been possible with the original version of TFEA [42, 45]. However, handling this type of equations using TFEA only became possible after the state–space TFEA extension in References [39].

The stability diagram and the convergence plots for Equation (52) at the point $(202.04, 28.38)$ are shown in Figure 6. In comparison with the scalar example, it can be seen that λ took longer to converge to $\mu*$ in all the used methods. However, Figure 6(b) shows that the conventional TFEA (circles) again converged linearly and had the slowest rate of convergence. In contrast, both the spectral element (dots) and the collocation approach (triangles) maintained their spectral convergence property. However, similar to the scalar example, the spectral element method converged faster than the collocation approach.

Figure 7(b) corresponds to the error associated with calculating the maximum Floquet multiplier in Equation (52) as a function of E and n (hp refinement). Each curve represents a constant n whereas E is varied in the horizontal axis between 1 and 24. Similar to Equation (48), convergence can be obtained by either increasing E or n. However, faster convergence rates can be obtained if both E and n are increased.

DOI: 10.1002/nme

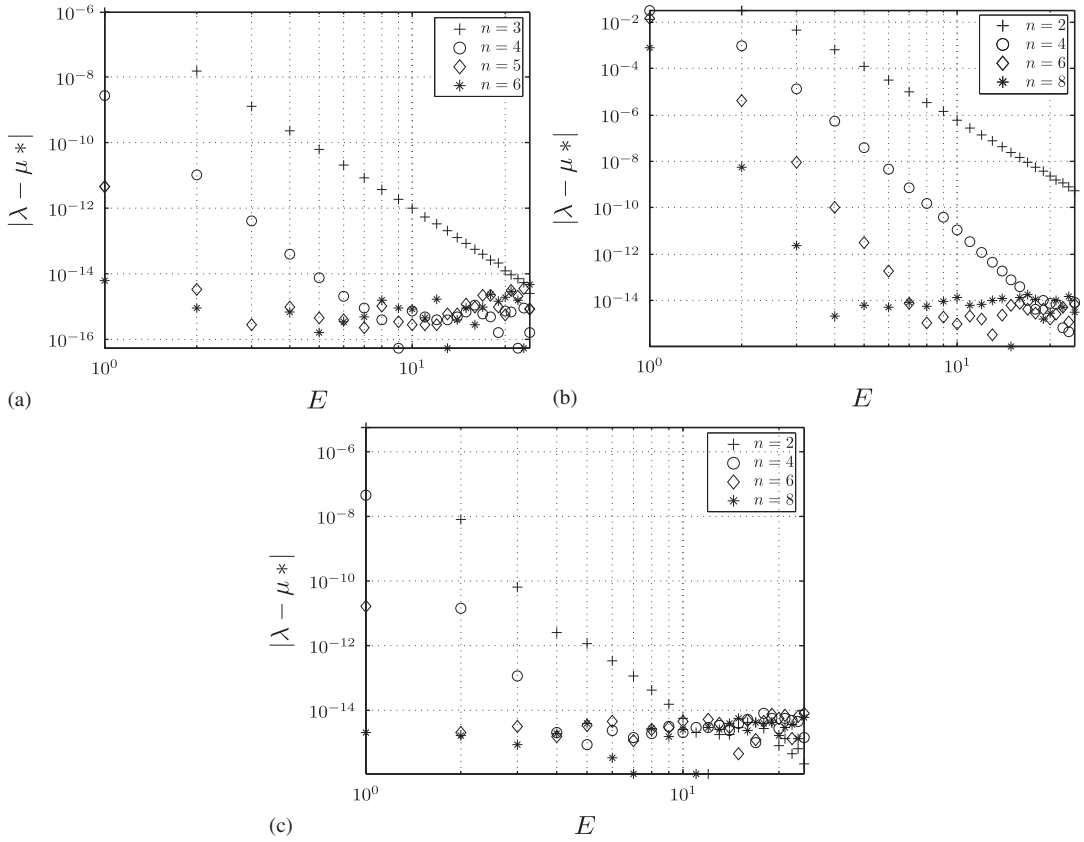

Figure 7. The absolute errors associated with calculating the maximum Floquet multiplier using the *hp* refinement capability of the spectral element method: (a) corresponds to the (α, β) point $(-1, 0.0754)$ in Equation (48); (b) corresponds to the (α, β) point $(202.04, 28.38)$ in Equation (52); and whereas (c) corresponds to the (Ω, δ) point $(1.16, 0.3)$ in Equation (56).

Using HPM with Equation (52) yields the set of equations

$$\rho^0 : v_0^{(3)} + \alpha \dot{v}_0 - (x_0^{(3)} + \alpha \dot{x}_0) = 0 \quad \text{where } v_0(0)=10, \ \ \dot{v}_0(0)=-1.6, \ \ \ddot{v}_0(0)=0.256 \tag{53}$$

$$\rho^1 : v_1^{(3)} + \alpha \dot{v}_1 + (x_0^{(3)} + \alpha \dot{x}_0) + \beta v_0(t-\tau) = 0 \quad \text{where } v_1(0)=\dot{v}_1(0)=\ddot{v}_1(0)=0 \tag{54}$$

$$\rho^2 : v_2^{(3)} + \alpha \dot{v}_2 + \beta v_k(t-\tau) = 0 \quad \text{where } v_k(0)=\dot{v}_k(0)=\ddot{v}_k(0)=0 \quad \text{for } k \geqslant 2 \tag{55}$$

where the chosen initial solution was $x_0(t) = 10\mathrm{e}^{-0.16t}$. The equilibria solution obtained with a second-order HPM is plotted with a dashed line in Figure 9(b) along with the simulated solution (solid line) and the spectral element solution (x). In generating the spectral element solution, the parameters $E = 3$ and $n = 6$ were used. Similar to Equation (48), it can be seen that both HPM and the spectral element approach show good agreement with numerical simulations.

A quantitative measure of the quality of the solutions obtained with the spectral element approach and HPM is shown in Figure 10 and Table III, respectively. Figures 10(c), (d) show the errors calculated using Equation (46) with the spectral element method. For each number of elements E, the order of the trial functions was varied between 2 and 40. It can be seen that for this example the approximate solution took longer to converge than Equation (48). Nevertheless, the convergence rate was exponential in each case and faster convergence rates were achieved by using more elements while maintaining the same order of trial functions.

DOI: 10.1002/nme

Table II. The relative errors associated with using different approximation orders of HPM to solve Equation (52).

HPM order	ε_2	ε_∞
0	4.48666×10^{-3}	6.45105×10^{-3}
1	1.75×10^{-4}	2.43775×10^{-4}
2	2.42496×10^{-4}	3.31655×10^{-4}

The errors associated with using HPM to find the equilibria solutions of Equation (52) are shown in Table II. The discrete errors were calculated using the mesh points of the spectral element approach with $E=3$ and $n=40$. It can be seen that although good results are obtained with HPM, a slight decrease in accuracy is observed when going from first- to second-order approximation. Moreover, comparing the accuracy of HPM with the spectral element errors, see Figures 10(c)–(d), shows that the spectral element method is more accurate.

8.4. A non-autonomous, time-periodic system

The previous two examples were for autonomous DDEs. However, the spectral element approach can also be used to study the stability of non-autonomous systems with time-periodic coefficients. For example, consider the system of coupled DDEs given by [69]:

$$\ddot{u}+2\zeta\dot{u}+(1-\delta\cos 2\Omega t)u-\delta\sin(2\Omega t)v=bu(t-T), \tag{56a}$$

$$\ddot{v}+2\zeta\dot{v}+(1+\delta\cos 2\Omega t)v-\delta\sin(2\Omega t)u=bv(t-T), \tag{56b}$$

$$u(s)=\sin(2\Omega s), \quad \text{for } s\in[-\tau,0], \tag{56c}$$

$$v(s)=\cos(2\Omega s), \quad \text{for } s\in[-\tau,0]. \tag{56d}$$

These equations describe the non-dimensionalized deflections of the midspan of an asymmetric shaft where ζ is damping, δ is a non-dimensional parameter describing the amount of asymmetry in the system, b is the non-dimensional feedback gain, Ω is the non-dimensional rotational frequency, and $T=\pi/\Omega$ is a constant delay. The delayed term is non-instantaneous or delayed feedback that is used to stabilize the shaft.

The results of the stability analysis of Equation (56) are shown in Figures 8(a)–(c). In these figures, the unstable region was shaded and the feedback gain was assigned the values $b=0$, $b=0.02$, and $b=0.04$, respectively. It can be seen that even small feedback gains can substantially change the stability boundaries and deteriorate the stable regions. Figure 8(d) shows the convergence plots for the magnitude of the maximum Floquet multiplier λ at the (Ω,δ) point $(1.16, 0.3)$ for the different methods. Specifically, the convergence is shown as a function of three quantities: (1) the number of elements in the conventional TFEA method (circles), (2) the number of Legendre collocation points (triangles), and (3) the order of the trial functions in the spectral element approach (dots).

Similar to the previous examples, it can be seen that the spectral element approach and the Legendre collocation approach had a spectral rate of convergence whereas the conventional TFEA converged last with a linear rate of convergence. Furthermore, the spectral element approach converged faster than the other two methods.

Figure 7(c) corresponds to the error associated with calculating the maximum Floquet multiplier in Equation (56) using hp refinement. In each curve, the order of the trial functions was held constant while the number of elements was varied between 1 and 24. It can be seen that increasing both the order of the trial functions and the number of elements leads to faster convergence. It can also be seen that although system (56) has more complicated coefficients than the

DOI: 10.1002/nme

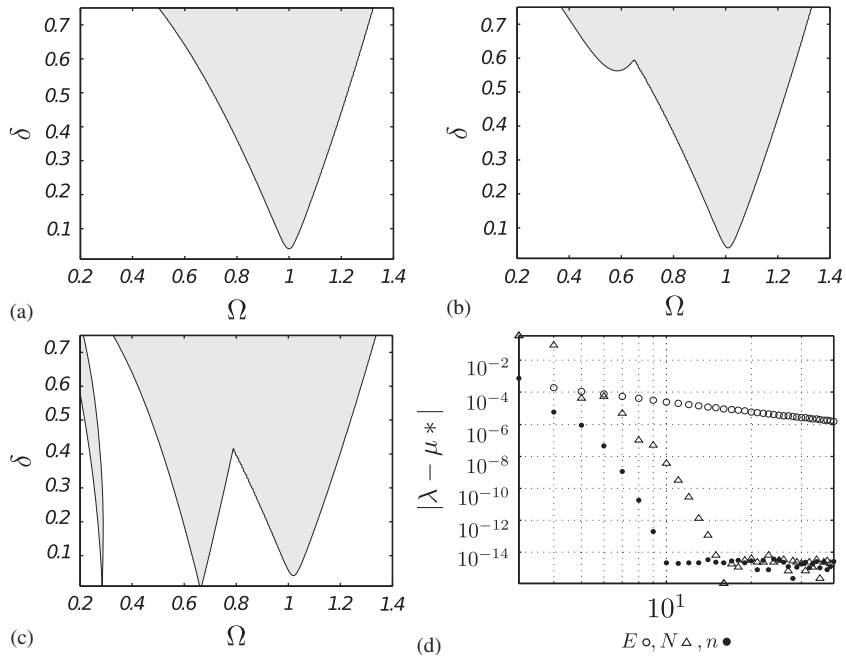

Figure 8. The stability diagram for Equation (56) and the spectral convergence plots for the (Ω, δ) point $(1.16, 0.3)$ in the parameter space. The parameters used were $\zeta = 0.02$ and (a) $b = 0$, (b) $b = 0.02$, and (c) $b = 0.04$. In graphs (a)-(c), the unstable regions are shaded whereas the stable regions are left unshaded. Graph (d) shows the convergence of the maximum eigenvalue as a function of: (1) the number of elements in the conventional TFEA approach (circles), (2) the number of collocation points in the Legendre collocation method (triangles), and (3) the order of the Lagrange trial functions (dots).

third-order DDE in (52), the maximum Floquet multiplier of Equation (56) converged faster. In fact, among all the cases considered here, the convergence rate for the third-order example was the slowest.

Using HPM with Equation (56) yields the set of equations

$$\rho^0 : \begin{cases} \ddot{w}_0 + 2\zeta\dot{w}_0 + w_0 - \mathscr{L}(u_0(t)) = 0 \\ \ddot{z}_0 + 2\zeta\dot{z}_0 + z_0 - \mathscr{L}(v_0(t)) = 0 \\ \text{where } w_0(0) = 0, \dot{w}_0(0) = 2\Omega, z_0(0) = 1, \dot{z}_0(0) = 0, \end{cases} \tag{57a}$$

$$\rho^1 : \begin{cases} \ddot{w}_1 + 2\zeta\dot{w}_1 + w_1 + \mathscr{L}(u_0(t)) - \delta\cos(2\Omega t)w_0 - \delta\sin(2\Omega t)z_0 - bw_0(t-\tau) = 0, \\ \ddot{z}_1 + 2\zeta\dot{z}_1 + z_1 + \mathscr{L}(v_0(t)) + \delta\cos(2\Omega t)z_0 - \delta\sin(2\Omega t)w_0 - bz_0(t-\tau) = 0, \\ \text{where } w_1(0) = 0, \dot{w}_1(0) = 0, z_1(0) = 0, \dot{z}_1(0) = 0, \end{cases} \tag{57b}$$

$$\rho^2 : \begin{cases} \ddot{w}_2 + 2\zeta\dot{w}_2 + w_2 - \delta\cos(2\Omega t)w_1 - \delta\sin(2\Omega t)z_1 - bw_1(t-\tau) = 0, \\ \ddot{z}_2 + 2\zeta\dot{z}_2 + z_2 + \delta\cos(2\Omega t)z_1 - \delta\sin(2\Omega t)w_1 - bz_1(t-\tau) = 0 \\ \text{where } w_2(0) = 0, \dot{w}_2(0) = 0, z_2(0) = 0, \dot{z}_2(0) = 0 \end{cases} \tag{57c}$$

DOI: 10.1002/nme

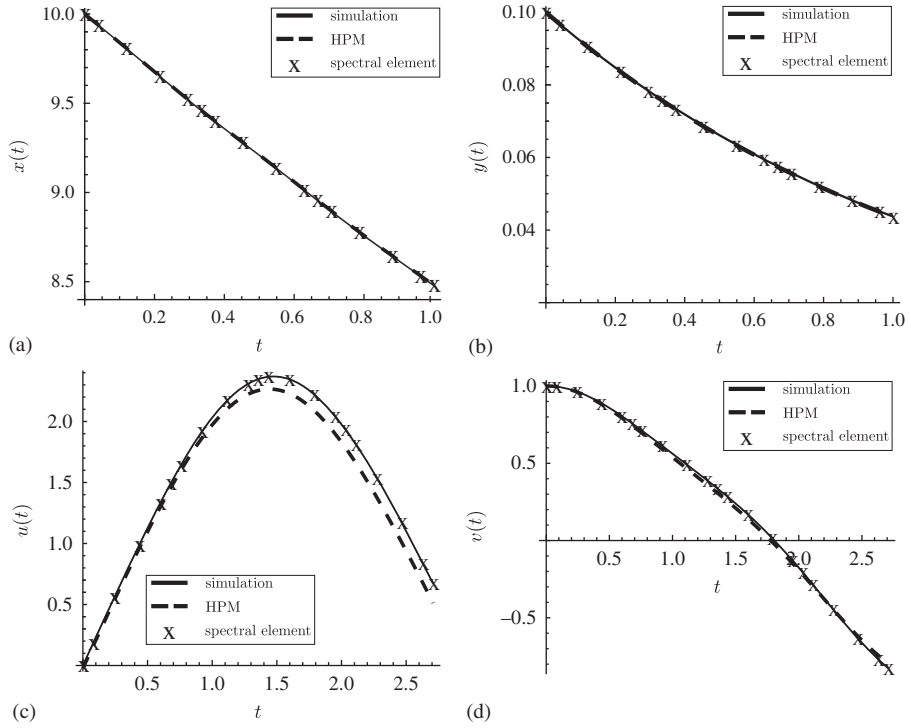

Figure 9. Comparison of the equilibria solutions obtained through numerical simulation (—), HPM (- -), and the spectral element method (x): (a) corresponds to Equation (48) while (b) corresponds to Equation (52); (c) and (d) correspond to the displacement in the u and v directions, respectively, in Equation (56). For the spectral element method, the parameters $E=3$ and $n=6$ were selected whereas a second-order HPM was used. Simulation results were obtained using the NDSolve command in Mathematica.

where the chosen initial solutions were $u_0(t)=4\sin(0.5\Omega t)$, $v_0(t)=\cos(0.5\Omega t)$ while the linear operator $\mathscr{L}$ was defined as:

$$\mathscr{L}(u_0)=-\Omega^2\sin(0.5\Omega t)+4\zeta\Omega\cos(0.5\Omega t)+4\sin(0.5\Omega t), \tag{58}$$

$$\mathscr{L}(v_0)=-\frac{\Omega^2}{4}\cos(0.5\Omega t)-\zeta\Omega\sin(0.5\Omega t)+\cos(0.5\Omega t). \tag{59}$$

The equilibria solutions for the displacement in the u and v direction are plotted in Figures 9(c), (d), respectively. The solutions obtained with a second-order HPM were plotted with a dashed line along with the simulated solution (solid line) and the spectral element solution (x). In generating the spectral element solution, the parameters $E=3$ and $n=6$ were used. Similar to Equation (48), it can be seen that although the spectral element approach showed good agreement with numerical simulations, HPM produced good results for the displacement in the u direction while the solution in the v direction diverged from numerical simulations.

A measure of the quality of the solutions obtained with the spectral element approach and HPM is shown in Figure 10 and Table II, respectively. Figures 10(e), (f) show the errors calculated for the displacement in the u direction whereas Figures 10(g) and (h) are for the displacement in the v direction. For each number of elements E, the order of the trial functions was varied between 2 and 40. Similar to the first two examples, the spectral element approach had an exponential rate of convergence that improved with increasing the number of elements and the order of the trial functions.

DOI: 10.1002/nme

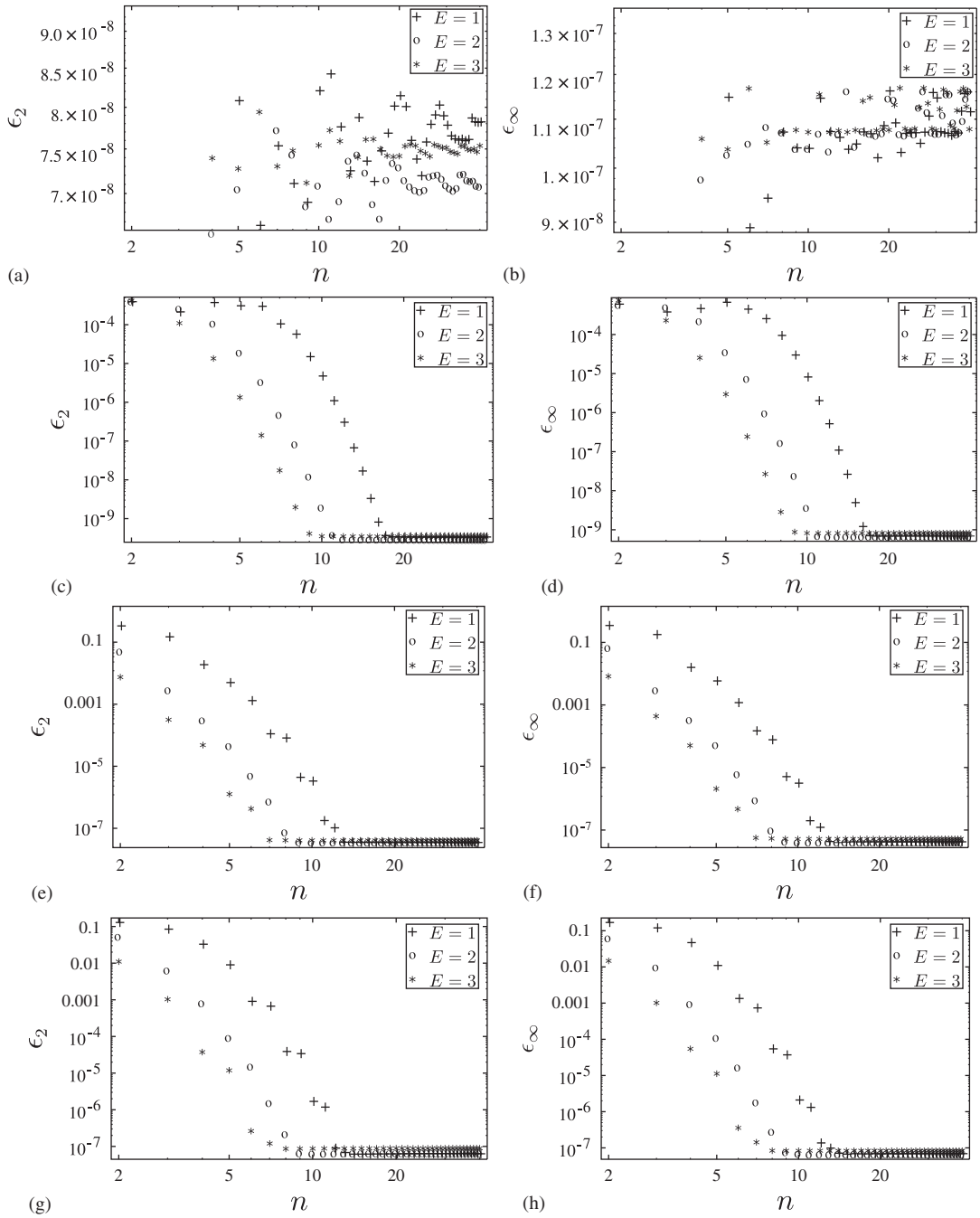

Figure 10. Error norms for the state variables in the case studies of Section 8. The first and second rows show the results for cases 1 and 2 corresponding to Equations (48) and (52), respectively. The errors associated with the third case study (Equation (56)) are shown in the third (u) and fourth (v) rows, respectively. For all cases, the number of elements E was varied between 1 and 3 while the order of the interpolating polynomial within each element n was varied 2 and 40.

The errors associated with using HPM to find the equilibria solutions of Equation (56) are shown in Table III. The discrete errors were calculated using the mesh points of the spectral element approach using $E = 3$ and $n = 40$. Comparing the accuracy of HPM with the spectral element errors showed that the spectral element method was more accurate, see Figures 10(e)–(h).

DOI: 10.1002/nme

9. CONCLUSIONS

This paper described a spectral element approach to study the stability and equilibria solutions of DDEs. In contrast to the prototypical TFEA, the described spectral element approach had exponential rates of convergence and allowed exploiting *hp*-convergence schemes. The described approach also avoided the limitations of analytical integrations in TFEA through employing highly accurate numerical quadratures—enabling the study of more complicated DDEs. The effectiveness of this new approach was compared with well-established methods in the literature using various case studies. Specifically, stability results were compared with the conventional TFEA and Legendre collocation methods whereas the equilibria solutions were compared with numerical simulations and the HPM solutions.

The developed spectral element approach avoided the limitations of the prototypical TFEA approach through (1) the use of the extrema of Legendre polynomials as optimum node locations within each element, (2) employing higher order trial functions obtained through the barycentric equations for Lagrange interpolation through the element nodes, and (3) using a Gauss quadrature rule to evaluate the weighted residual integrals. These features gave the current approach the advantage of evaluating the weighted residual integrals and populate the global matrices using only the information from the temporal mesh and the state–space matrices.

The spectral element approach was also shown to produce block matrices whose structure could be employed in sparse eigenvalue solvers for faster stability calculations. We also explored the connection between the spectral element method and collocation techniques in Section 6 and included comments on the convergence of the spectral element approach.

We used a set of case studies to compare the stability results obtained with the spectral element method against the conventional state–space TFEA and Legendre collocation. The resulting stability diagrams to which all the methods converged were shown in Figures 5(a) and 6(a) as well as Figures 8(a)–(c). The maximum Floquet multiplier at a point near the stability boundary was also calculated through these methods and compared with a reference value obtained using a high-order Legendre collocation.

The absolute errors between the calculated and the reference multipliers for each case were plotted on a log-log scale in Figures 5(b), 6(b), and 8(d). The results showed that in contrast to the linear rate of convergence in the conventional state–space TFEA, both the spectral element method and the collocation approach had spectral rates of convergence. Further ,the spectral element approach had superior rates of convergence in comparison with the Legendre collocation method. The *hp* refinement capability in the spectral element approach was shown in Figure 7 where the absolute error in calculating the maximum Floquet multiplier was plotted as a function of the number of elements and the order of the trial functions.

We also compared the equilibria solutions obtained using the spectral element method to analytically and numerically computed solutions. The analytical approximate solutions were obtained using HPM whereas the basis of comparison were the numerical simulations obtained with Mathematica's NDSolve command. The solutions obtained using these different methods were compared in Figure 9 for the various case studies. It was found that qualitatively both the spectral element approach and HPM agreed well with numerical simulations.

To quantify the errors associated with the approximate solutions, two relative error measures were defined based on the discrete ℓ_2 and ℓ_∞ norms. For the spectral element approach, the errors were plotted as a function of the number of elements and the order of the trial functions in Figure 10. Similarly, the errors associated with using first- and second-order HPM approximations were tabulated in Tables I–III. Comparing the resulting errors, it was found that although it can be relatively easier to use HPM, the spectral element approach led to significantly more accurate results as the order of the trial functions was increased.

To summarize, the developed spectral element approach for DDEs is more robust than the conventional TFEA method and it allows *hp* refinement which was lacking in the conventional approach. Further, our results revealed that the presented approach could have higher rates of convergence than both collocation methods and the HPM. This makes the current approach more

DOI: 10.1002/nme

Table III. The relative errors associated with using different approximation orders of HPM to solve Equation (56).

	u		v	
HPM order	ε_2	ε_∞	ε_2	ε_∞
0	8.54451×10^{-1}	1.40505	7.39515×10^{-1}	8.26451×10^{-1}
1	1.09676×10^{-1}	1.42607×10^{-1}	5.96292×10^{-2}	9.58244×10^{-2}
2	5.42773×10^{-2}	6.31958×10^{-2}	4.01561×10^{-2}	5.55211×10^{-2}

suitable for stability studies of a larger class of problems including DDEs with complicated time-dependent coefficients as well as DDEs with multiple and distributed delays.

ACKNOWLEDGEMENTS

Support from U.S National Science Foundation with grant no. CMMI-0900266 is gratefully acknowledged.

REFERENCES

1. Loiseau J, Michiels W, Niculescu SI, Sipahi R (eds). *Topics in Time Delay Systems Analysis*: *Algorithm and Control*. Springer: Berlin, 2009; DOI: 10.1007/978-3-642-02897-7.
2. Butcher E, Bobrenkov O, Bueler E, Nindujarla P. Analysis of milling stability by the Chebyshev collocation method: algorithm and optimal stable immersion levels. *Journal of Computational and Nonlinear Dynamics* 2009; **4**(3):031003. DOI: 10.1115/1.3124088.
3. Bobrenkov O, Khasawneh F, Butcher E, Mann B. Analysis of milling dynamics for simultaneously engaged cutting teeth. *Journal of Sound and Vibration* 2010; **329**(5):585–606. DOI: 10.1016/j.jsv.2009.09.032.
4. Krauskopf B. Unlocking dynamical diversity: optical feedback effects on semiconductor lasers. *Bifurcation Analysis of Lasers with Delay*. Wiley: NJ, 2005; 147–183.
5. Shahverdiev E, Bayramov P, Shore K. Cascaded and adaptive chaos synchronization in multiple time-delay laser systems. *Chaos*, *Solitons and Fractals* 2009; **42**(1):180–186. DOI: 10.1016/j.chaos.2008.11.004.
6. Chicone C, Feng Z. Synchronization phenomena for coupled delay-line oscillators. *Physica D*: *Nonlinear Phenomena* 2004; **198**(3–4):212–230. DOI: 10.1016/j.physd.2004.08.027.
7. Sipahi R, Atay F, Niculescu SI. Stability of traffic flow behavior with distributed delays modeling the memory effects of the drivers. *SIAM Journal on Applied Mathematics* 2007; **68**(3):738–759. DOI: 10.1137/060673813.
8. Michiels W, Morrescu CI, Niculescu SI. Consensus problems with distributed delays, with application to traffic flow models. *SIAM Journal on Control and Optimization* 2009; **48**(1):77–101. DOI: 10.1137/060671425.
9. Stépán G, Kollar L. Balancing with reflex delay. *Mathematical and Computer Modelling* 2000; **31**:199–205.
10. Cabrera J, Milton J. On-off intermittency in a human balancing task. *Physical Review Letters* 2002; **89**(15):158–702. DOI: 10.1103/PhysRevLett.89.158702.
11. Stépán G. *Retarded Dynamical Systems*: *Stability and Characteristic Functions*. Wiley: New York, 1989.
12. Hale JK, Lunel SV. *Introduction to Functional Differential Equations*. Springer: New York, 1993.
13. Breda D, Maset S, Vermiglio R. Pseudospectral differencing methods for characteristic roots of delay differential equations. *SIAM Journal on Scientific Computing* 2005; **27**(2):482–495.
14. Sun JQ, Song B. Optimal control of time-delayed linear systems with the method of continuous time approximation. *ASME Conference Proceedings*, vol. 2008(43321), 2008; 317–322. DOI: 10.1115/SMASIS2008-388.
15. Sun JQ. A method of continuous time approximation of delayed dynamical systems. *Communications in Nonlinear Science and Numerical Simulation* 2009; **14**(4):998–1007.
16. Olgac N, Sipahi R. A unique methodology for chatter stability mapping in simultaneous machining. *Journal of Manufacturing Science and Engineering* 2005; **127**:791–800. DOI: 10.1115/1.2037086.
17. Sipahi R, Olgac N. Complete stability analysis of neutral-type first order two-time delay systems with cross-talking delays. *SIAM Journal on Control Optimization* 2006; **45**(3):957–971.
18. He JH. Homotopy perturbation technique. *Computer Methods in Applied Mechanics and Engineering* 1999; **178**(3–4):257–262. DOI: 10.1016/S0045-7825(99)00018-3.
19. He JH. A coupling method of a homotopy technique and a perturbation technique for non-linear problems. *International Journal of Non-linear Mechanics* 2000; **35**(1):37–43. DOI: 10.1016/S0020-7462(98)00085-7.
20. He JH. Homotopy perturbation method: a new nonlinear analytical technique. *Applied Mathematics and Computation* 2003; **135**(1):73–79. DOI: 10.1016/S0096-3003(01)00312-5.
21. He JH. Homotopy perturbation method for solving boundary value problems. *Physics Letters A* 2006; **350**(1–2):87–88. DOI: 10.1016/j.physleta.2005.10.005.

22. He JH. Variational iteration method—a kind of non-linear analytical technique: some examples. *International Journal of Non-linear Mechanics* 1999; **34**(4):699–708. DOI: 10.1016/S0020-7462(98)00048-1.
23. He JH, Wu X. Variational iteration method: new development and applications. *Computers and Mathematics with Applications* 2007; **54**:881–894. DOI: 10.1016/j.camwa.2006.12.083.
24. He JH, Wu G, Austin F. The variational iteration method which should be followed. *Nonlinear Science Letters A—Mathematics Physics and Mechanics* 2010; **1**(1):1–30.
25. He JH. Variational iteration method for delay differential equations. *Communications in Nonlinear Science and Numerical Simulation* 1997; **2**(4):235–236. DOI: 10.1016/S1007-5704(97)90008-3.
26. He JH. Periodic solutions and bifurcations of delay-differential equations. *Physics Letters A* 2005; **347**(4–6):228–230. DOI: 10.1016/j.physleta.2005.08.014.
27. Yu ZH. Variational iteration method for solving the multi-pantograph delay equation. *Physics Letters A* 2008; **372**(43):6475–6479. DOI: 10.1016/j.physleta.2008.09.013.
28. Shakeri F, Dehghan M. Solution of delay differential equations via a homotopy perturbation method. *Mathematical and Computer Modelling* 2008; **48**(3–4):486–498. DOI: 10.1016/j.mcm.2007.09.016.
29. Tatari M, Dehghan M. On the convergence of he's variational iteration method. *Journal of Computational and Applied Mathematics* 2007; **207**(1):121–128. DOI: 10.1016/j.cam.2006.07.017. Special Issue: Variational Iteration Method—Reality, Potential, and Challenges.
30. He JH. *Perturbation Methods*: *Basic and Beyond*. Elsevier: Amsterdam, 2006.
31. Hesameddini E, Latifizadeh H. An optimal choice of initial solutions in the homotopy perturbation method. *International Journal of Nonlinear Sciences and Numerical Simulation* 2009; **10**:1389–1398.
32. Insperger T, Stépán G. Semi-discretization method for delayed systems. *International Journal for Numerical Methods in Engineering* 2002; **55**:503–518.
33. Insperger T, Stépán G. Updated semi-discretization method for periodic delay-differential equations with discrete delay. *International Journal for Numerical Methods* 2004; **61**:117–141.
34. Engelborghs K, Luzyanina T, Int Hout KJ, Roose D. Collocation methods for the computation of periodic solutions of delay differential equations. *SIAM Journal on Scientific Computing* 2000; **22**:1593–1609.
35. Luzyanina T, Engelborghs K. Computing floquet multipliers for functional differential equations. *International Journal of Bifurcation and Chaos* 2002; **12**(12):2977–2989.
36. Engelborghs K, Doedel E. Stability of piecewise polynomial collocation for computing periodic solutions of delay differential equations. *Numerische Mathematik* 2002; **91**:627–648.
37. Butcher E, Ma H, Bueler E, Averina V, Szabó Z. Stability of linear time-periodic delay-differential equations via Chebyshev polynomials. *International Journal for Numerical Methods in Engineering* 2004; **59**:895–922.
38. Barton D, Krauskopf B, Wilson R. Collocation schemes for periodic solutions of neutral delay differential equations. *Journal of Difference Equations and Applications* 2006; **12**(11):1087–1101. DOI: 10.1080/10236190601045663.
39. Mann B, Patel B. Stability of delay equations written as state space models. *Journal of vibration and control* 2010; **16**:1067–1085. DOI: 10.1177/1077546309341111.
40. Boyd JP. *Chebyshev and Fourier Spectral Methods*. Dover Publications: New York, 2001.
41. Khasawneh F, Mann B, Butcher E. Comparison between collocation methods and spectral element approach for the stability of periodic delay systems. *Ninth IFAC Workshop on Time Delay Systems*, Prague, Czech Republic, IFAC-TDS2010-KF-552, 2010.
42. Mann BP, Young KA. An empirical approach for delayed oscillator stability and parametric identification. *Proceedings of the Royal Society A* 2006; **462**:2145–2160.
43. Sims ND, Mann B, Huyanan S. Analytical prediction of chatter stability for variable pitch and variable helix milling tools. *Journal of Sound and Vibration* 2008; **317**:664–686.
44. Khasawneh F, Mann B, Insperger T, Stépán G. Increased stability of low-speed turning through a distributed force and continuous delay model. *Journal of Computational and Nonlinear Dynamics* 2009; **4**(4):041003.
45. Bayly PV, Halley JE, Mann BP, Davis MA. Stability of interrupted cutting by temporal finite element analysis. *Journal of Manufacturing Science and Engineering* 2003; **125**:220–225.
46. Reddy J. *An Introduction to the Finite Element Method* (2nd edn). McGraw-Hill, Inc.: New York, NY, 1993.
47. Tlusty J. *Manufacturing Processes and Equipment* (1st edn). Prentice-Hall: Upper Saddle River, NJ, 2000.
48. Chirikalov VA. Computation of the differentiation matrix for the Hermite interpolating polynomials. *Journal of Mathematical Sciences* 1994; **68**(6):766–770. DOI: 10.1007/BF01672645.
49. Leader JJ. *Numerical Analysis and Scientific Computation* (1st edn). Addison-Wesley: Reading, MA, 2004.
50. Schneider C, Werner W. Hermite interpolation: the barycentric approach. *Computing* 1991; **46**(1):35–51. DOI: 10.1007/BF02239010.
51. Corless R, Shakoori A, Aruliah D, Gonzalez-Vega L. Barycentric Hermite interpolants for event location in initial-value problems. *Journal of Numerical Analysis*, *Industrial and Applied Mathematics* 2007; **1**(1):1–14.
52. Berrut J, Trefethen LN. Barycentric Lagrange interpolation. *SIAM Review* 2004; **46**(3):501–517.
53. Bloom T, Lubinsky DS, Stahl H. Interpolatory integration rules and orthogonal polynomials with varying weights. *Numerical Algorithms* 1992; **3**(1):55–65.
54. Vu TH, Deeks AJ. Use of higher-order shape functions in the scaled boundary finite element method. *International Journal for Numerical Methods in Engineering* 2006; **65**:1714–1733.
55. Higham N. The numerical stability of barycentric Lagrange interpolation. *IMA Journal of Numerical Analysis* 2004; **24**(4):547–556. DOI: 10.1093/imanum/24.4.547.

56. Parter S. On the Legendre–Gauss–Lobatto points and weights. *Journal of Scientific Computing* 1999; **14**(9):347–355.
57. Eslahchi M, Masjed-Jamei M, Babolian E. On numerical improvement of Gauss–Lobatto quadrature rules. *Applied Mathematics and Computation* 2005; **164**(3):707–717. DOI: 10.1016/j.amc.2004.04.113.
58. Ma H, Butcher EA, Bueler E. Chebyshev expansion of linear and piecewise linear dynamic systems with time delay and periodic coefficients under control excitations. *Journal of Dynamic Systems, Measurement, and Control* 2003; **125**:236–243.
59. Deshmukh V, Ma H, Butcher EA. Optimal control of parametrically excited linear delay differential systems via Chebyshev polynomials. *Optimal Control Applications and Methodology* 2006; **27**:123–136.
60. Elnagar G, Kazemi MA, Razzaghi M. The pseudospectral Legendre method for discretizing optimal control problems. *IEEE Transactions on Automatic Control* 1995; **40**(10):1793–1796.
61. Fernandez F, Davies J, Zhu S, Lu Y. Sparse matrix eigenvalue solver for finite element solution of dielectric waveguides. *Electronics Letters 26* 1991; **27**(20):1824–1826. DOI: 10.1049/el:19911133.
62. Insperger T, Mann BP, Stépán G, Bayly PV. Stability of up-milling and down-milling, part 1: alternative analytical methods. *International Journal of Machine Tools and Manufacture* 2003; **43**:25–34.
63. Nia SH, Ranjbar A, Ganji D, Soltani H, Ghasemi J. Maintaining the stability of nonlinear differential equations by the enhancement of hpm. *Physics Letters A* 2008; **372**(16):2855–2861. DOI: 10.1016/j.physleta.2007.12.054.
64. Bellman R, Cooke K. *Differential-difference Equations*. Academic Press Inc.: New York, 1963.
65. Claeyssen J. Effect of delays on functional differential equations. *Journal of Differential Equations* 1976; **20**(2):404–440. DOI: 10.1016/0022-0396(76)90117-0.
66. Hale J, Huang W. Global geometry of the stable regions for two delay differential equations. *Journal of Mathematical Analysis and Applications* 1993; **178**:344–362.
67. Ma X, Wei L, Guo Z. He's homotopy perturbation method to periodic solutions of nonlinear jerk equations. *Journal of Sound and Vibration* 2008; **314**(1–2):217–227. DOI: 10.1016/j.jsv.2008.01.033.
68. Rauch L. Oscillations of a third-order non-linear autonomous system. *Contributions to the Theory of Non-linear Oscillations*, Annals of Mathematics Studies, vol. 20. Princeton University Press: NJ, 1950; 39–88.
69. Yamamoto T, Ishida Y. *Linear and Nonlinear Rotor Dynamics*. Wiley: New York, 2001.